RESEARCH ARTICLE | FEBRUARY 07 2024

The role of porous structure on airfoil turbulence interaction noise reduction

L. Bowen ; A. Celik ; M. F. Westin ; M. Azarpeyvand

Physics of Fluids 36, 025113 (2024)
https://doi.org/10.1063/5.0186501

Physics of Fluids ARTICLE pubs.aip.org/aip/pof

The role of porous structure on airfoil turbulence interaction noise reduction

Cite as: Phys. Fluids **36**, 025113 (2024); doi: 10.1063/5.0186501
Submitted: 6 November 2023 · Accepted: 10 January 2024 ·
Published Online: 7 February 2024

L. Bowen,[1,a)] A. Celik,[2] M. F. Westin,[3] and M. Azarpeyvand[1]

AFFILIATIONS

[1]Faculty of Engineering, University of Bristol, Bristol BS8 1TR, United Kingdom
[2]Aerospace Engineering, Swansea University, Swansea SA1 8EN, United Kingdom
[3]Embraer, Sáo José dos Campos, 12227-901, Brazil

[a)]Author to whom correspondence should be addressed: luke.bowen@bristol.ac.uk

ABSTRACT

Experiments are performed to investigate the effect of porous treatment structure used at the leading edge on the aerodynamic and aeroacoustic characteristics of a National Advisory Committee for Aeronautics (NACA) 0012 airfoil. Three different triply periodic minimal surface porous structures of constant porosity are studied to explore their effect on the flow field and the relationship between airfoil response and far-field noise. The results show that the ratio between the porous structure pore size and the length scale of the turbulent flow plays an important role in the noise reduction capability of a porous leading edge. Changes to the turbulent flow properties in the vicinity of the airfoil are assessed to characterize the contributing physical behavior responsible for far-field noise manipulation. Velocity field analysis in front of the leading edge demonstrates a pronounced difference among porous structures. Furthermore, close to the airfoil surface and off from the stagnation line, all porous leading edges demonstrate a marked reduction in the low-frequency content of the velocity fluctuations. These results demonstrate the importance of the airfoil leading edge region and not just the stagnation line. The strong link evident in pressure–velocity coherence analysis of the solid airfoil is broken by the introduction of the porous leading edge. Furthermore, the porous leading edges reduce the near-field to far-field pressure coherence in both magnitude and frequency range.

I. INTRODUCTION

In the search for a sustainable future, noise pollution will continue to be a societal and environmental challenge. Turbulence interaction noise, generated due to the interaction of the leading edge with the incoming turbulent flow, is one of the dominant noise sources for electric fan engines, turbofans, and turbine engines employ guide vanes or flow straightening devices. These devices can generate significant amounts of noise due to the turbulent flow impinging on the leading edge of the device.

Interest in airfoil turbulence interaction noise began to gather interest following the fundamental study by Amiet.[1] The eminent Amiet model[1] is a prediction tool for turbulence interaction noise which works in two parts, first linearized theory is utilized to calculate the aerodynamic response of the incident gust on an airfoil, followed by calculation of the unsteady lift propagation to the far-field whilst considering for mean flow and scattering effects. Since, interest has been focused on the quantification of the flow conditions and geometric properties that influence turbulence interaction noise.

The effect of the angle of attack on the turbulence interaction noise has previously been shown to be insignificant,[2] yet there is a profound change in the airfoil response function, which does not have a dramatic effect on noise generation.[3] Furthermore, Celik *et al.*[4,5] demonstrated that the lack of sensitivity to the angle of attack extends to the lift and drag spectra too. Airfoil geometry studies in the context of turbulence interaction noise indicate that airfoil thickness and camber play important roles in noise generation.[6–8] Equally important, the turbulent inflow has a profound impact on turbulence interaction noise; specifically, an increase in turbulence length scale and turbulence intensity results in increased noise spectra levels.[9,10]

Reduction of aerodynamically generated noise is proven to be effective through the means of passive flow control, be that through the use of serrations[11–17] or porous materials.[18–24] Serrations have been the subject of many studies for the reduction of turbulence interaction noise due to their ease of implementation;[16,25–28] however, they require a fundamental change to the design of the airfoil geometry at the leading edge. The use of a porous treatment for the reduction of turbulence interaction noise results in the preservation of existing airfoil geometry with a change of the main material's porosity. One of the more notable first studies into the use of porous materials for the reduction of aerodynamically generated noise was the use of a porous fan blade.[29] The study demonstrated a reduction in the noise by 5 dB; however, a reduction of the fan static efficiency was also reported.[29]

Early numerical work considered the concept of a porous leading edge on a rotating blade.[30] Lee[30] conducted an investigation using blade vortex interaction (BVI) method to study the acoustic wave propagation of a solid and porous leading edge of a rotating blade. A parametric study of porosity effects is conducted, and it is concluded that a porous leading edge can reduce BVI noise by up to 30%. The physical mechanism for the reduction is the exchange of mass and momentum through the surface due to the porous boundary condition.[30]

Further work on the use of porous materials for the reduction of turbulence interaction was conducted by Tinetti *et al.*[31] By using the setup approach of wake-stator noise computational fluid dynamics (CFD) simulation, Tinetti *et al.*[31] used leading edge porosity to study the reduction of wake-stator noise. The study finds that the location of the implementation of the porous treatment is of prior importance, and the porosity is secondary. The location of which is centered around the chordwise location of 15% and 20% of the chord on the suction and pressure sides, respectively. In terms of the effect of aerodynamically generated sound, reductions of turbulence interaction of up to 2.5 dB are observed, but when increased thickness noise is considered, the noise reduction due to the porous leading edge reduces to 1 dB.

More recently, Geyer *et al.*[32] conducted the first study with porous airfoils used for turbulence interaction noise reduction. The study focused on fully porous airfoils utilizing commercially available porous foams of varying levels of porosity and permeability and found that increasing permeability led to significant noise reduction despite aerodynamic losses. The noise reduction mechanism is attributed to a decrease in the kinetic energy of the turbulent structures impinging on the airfoil leading edge due to hydrodynamic absorption. Further studies have highlighted the self-noise reduction capabilities of using porous airfoils.[32–34] Roger *et al.*[35] conducted experiments with a NACA-0012 airfoil profile, with a rigid flat plate center covered with porous absorbing material and a wire mesh skin. The airfoil was subject to turbulent flow generated by grids as well as in a tandem configuration with cylinders of different diameters. The reduction in turbulence interaction noise due to the porous airfoil was approximately 5 dB over a range of frequencies. In addition to the experimental observations, modeling of the problem was also conducted by solving the potential flow equation in the time domain with the use of a panel method. By using this approach to conduct analysis of the airflow resistance (permeability) of the material, it is found that increasing the permeability led to further reduction in the noise. In an extension of this work, Roger and Moreau[36] reported reductions in turbulence interaction noise between a grid turbulence flow and a porous NACA 0012 airfoil made up of wire wool of between 4 and 8 dB.

In an effort to further understand the reduction of turbulence interaction noise with a porous treatment, Satcunanathan *et al.*[37] carried out a simulation of the problem with a cylinder generating the turbulent flow. Large eddy simulation (LES) of a rod and a NACA0024 airfoil in a solid and porous configuration is conducted, and it is reported that the porous airfoil manipulates the mean flow and a reduction in the near-field hydrodynamic fluctuations is evident. These simulations also report a small reduction in the far-field noise which is owed to the porous material selection, and the authors suggest a different type of porous material may yield greater noise reduction.

Zamponi *et al.*[38] demonstrated through an experimental and numerical study that reductions of rod–airfoil interaction noise with a porous airfoil are achieved through a reduction in the upwash component in front of the airfoil leading edge are responsible for a reduction in far-field noise. By limiting the porous extent of the airfoil to the leading edge region, it has been demonstrated that grid-generated turbulence interaction noise with an airfoil with perforations is reduced by up to 8 dB.[39]

Another form of turbulence interaction noise can be considered a rotational wake interacting with a pylon. Sinnige *et al.*[40] consider this configuration, with a propeller and nacelle mounted to a pylon, where the pylon has a porous treatment. Far-field noise analysis using acoustic beamforming results in a reduction in the noise in the pylon region, where performance of the noise reduction increases with cavity depth, yet the aerodynamic penalty also increases. Sinnige *et al.*[40] note that the aerodynamic to aeroacoustic performance trade-off should be carefully considered when designing for this configuration.

Multiple studies[41,42] examined a flat plate in a turbulent stream, both experimentally and analytically. The flat plate featured perforations downstream of the leading edge, which effectively reduced the flat plate chord, resulting in an overall noise reduction. Bowen *et al.*[43] demonstrated that using both metal foams and 3D-printed geometries can reduce grid-generated turbulence interaction noise by up to 5 dB at low frequencies. However, as with other studies into the use of porous materials for flow control,[20,21,32] a high-frequency penalty is associated with the effective surface roughness of the porous material.[19] However, the high-frequency noise increase can be partially reduced with a flow permeable cover.[43] Advances in additive manufacturing have allowed for the use of more tailored porous treatments, where porosity can be controlled more easily. Ocker *et al.*[44] demonstrated that using specifically designed porous architecture at the leading edge of a fan blade in the wake of grid-generated turbulence can reduce interaction noise by up to 10 dB, with aerodynamic losses up to 30%. More recently, Bowen *et al.*[45] demonstrated the effect of porosity on the reduction of turbulence interaction noise, suggesting that porosity of at least 50% is required to observe substantial noise reduction. Furthermore, the study demonstrated increased spanwise coherence of velocity fluctuations at the point of hydrodynamic penetration into the porous leading edge when compared to the behavior of a solid leading edge.

It is clear from the literature that a leading edge porous treatment can reduce the low-to-mid frequency noise generated by turbulence interaction with an airfoil, with the penalty of increased high-frequency noise. In general, the literature uses porous materials that are considered "off the shelf" and have little control over the porosity. Furthermore, the literature lacks detailed near-surface measurements of airfoils fitted with a porous leading edge in addition to coherence analysis for such a configuration. This study sets out to assess the use of mathematically defined porous structures for the reduction of turbulence interaction noise. Furthermore, the study aims to further understand the complexities of the flow around a porous leading edge that lead to changes in the far-field noise. This is achieved by studying the turbulent flow interactions over various mathematically defined porous structures at the airfoil leading edge. The paper is organized so that the wind tunnel, measurement setup, porous structure design, and airfoil are described in Sec. II. The results and discussion of the far-field noise, turbulent flow interactions, and the link between both of these physical quantities are presented in Sec. III. Section IV concludes the findings of the paper.

II. MEASUREMENT SETUP

This section outlines the experimental setup used in this airfoil turbulence interaction noise study. Details of the aeroacoustic facility, turbulence generation, and the airfoil model are explained. Furthermore, the design, manufacture, and properties of the porous leading edges are explained as well as the experimental apparatus and measurement techniques used in the study.

A. Wind tunnel and model

The airfoil turbulence interaction noise experiments were performed in the University of Bristol Aeroacoustic Facility, which is a closed-circuit, open-jet anechoic wind tunnel. The chamber has physical dimensions of $6.7 \times 4.0 \times 3.3\ \text{m}^3$ and is anechoic down to 160 Hz.[46] Figure 1 displays a schematic of the wind tunnel contraction with the turbulence grid mounted in the contraction nozzle and the airfoil mounted within side plates, 350 mm downstream of the contraction nozzle outlet. The contraction nozzle outlet has physical dimensions of 500 mm in width and 775 mm in height, which allows for a steady operation from 5 to 45 m/s and a normal turbulence intensity level below 0.2%.[46]

This study was conducted with a NACA 0012 profile airfoil that features an interchangeable leading edge, with a span of 600 mm and chord of 200 mm, see Fig. 2. The airfoil was manufactured in one piece using the additive manufacturing technique of selective laser sintering (SLS) from polyamide. The airfoil was designed to be highly instrumented for the measurement of both aerodynamic and aeroacoustic phenomena in the form of static pressure and unsteady surface pressure. Instrumentation was achieved by the use of brass tubes with 0.4 mm pressure holes which were installed with two part epoxy resin and smoothed to the surface of the airfoil. The airfoil instrumentation consists of 48 static pressure taps and 88 unsteady surface pressure taps. The 48 static pressure taps were connected to two Chell MicroDaq-32 pressure scanners. The pressure coefficient results for

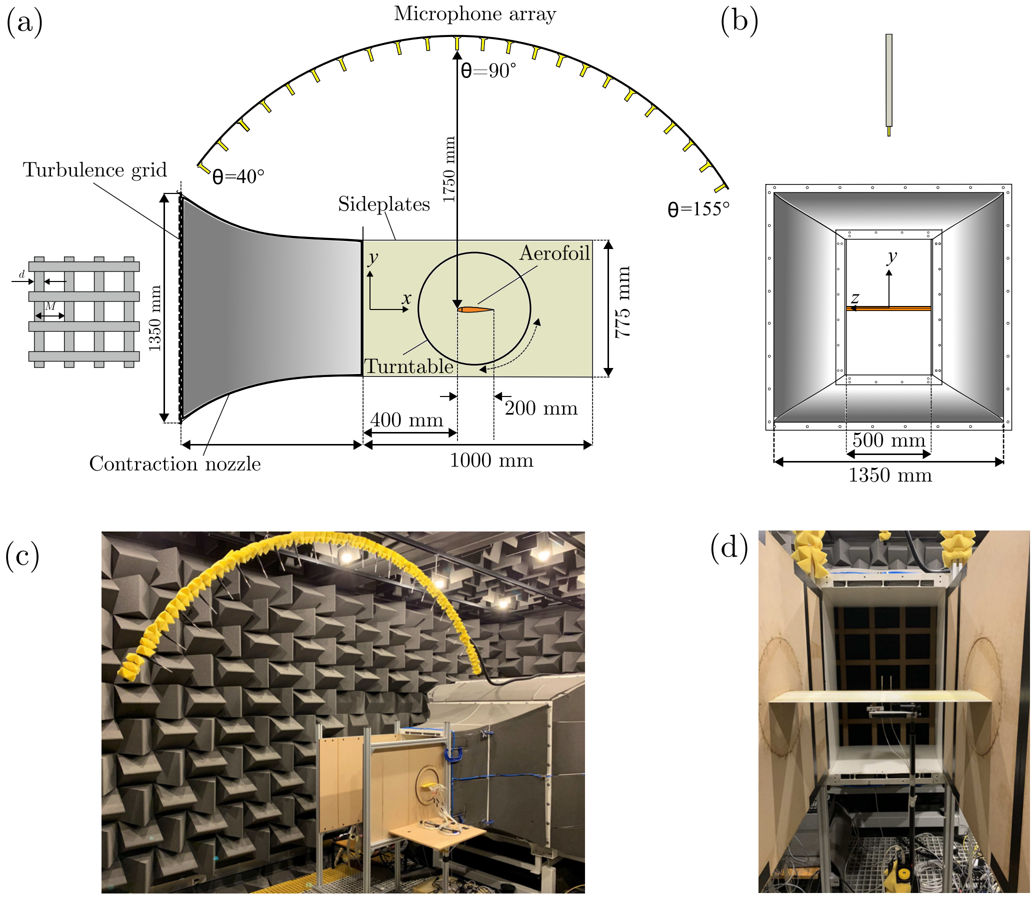

FIG. 1. Schematics of the experimental setup; [(a) and (b)] side and front view with details of the turbulence grid and far-field microphone array, [(c) and (d)] the images of the aeroacoustic wind tunnel facility and setup.

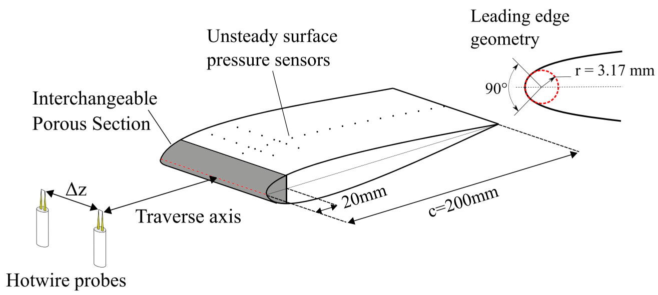

FIG. 2. Schematics of the NACA 0012 airfoil with an interchangeable leading edge and locations of the pressure sensors with a depiction of the tandem hot-wire configuration.

this configuration are omitted as they are previously reported.[23,24,43] The surface pressure taps were connected in a remote sensing configuration using Panasonic WM-61A microphones, which have a reliable frequency range between $10 < f < 6000$ Hz.[47,48] The Panasonic WM-61A microphones measure the pressure fluctuations at the pressure tap via a brass tube which is connected to the microphone in a custom-made holder that is acoustically terminated. More information regarding this measurement technique can be found in the literature.[47–49] All surface pressure microphones were calibrated using a white noise signal and calibrated in both magnitude and phase referenced to a single GRAS 40PL microphone, which was calibrated using a GRAS 42AA pistonphone calibrator. The calibration procedure utilizes a loudspeaker, connected to a cone with an acoustic termination and two perpendicular holes for the remote sensor and the reference GRAS microphone to be equidistant from the white noise source. The procedure for the calibration was established by Mish,[50] and further details of the exact procedure are presented previously.[51,52] Unsteady surface pressure measurements were performed via remote sensing and were sampled at a frequency of 2^{15} Hz for 32 s. Static pressure measurements were obtained using two Chell MicroDaq-32 pressure acquisition systems and were sampled for 32 s at a frequency of 1000 Hz.

B. Far-field measurement

The far-field noise was measured using a far-field microphone array as illustrated in Fig. 1. The array consists of 23 GRAS 40PL microphones, arranged at 5° increments between polar angles of $\theta = 40°$ and 155° to enable directivity measurements. The arc was located 1.75 m above the airfoil, with the microphone at $\theta = 90°$ located directly above the leading edge of the airfoil. All microphones were calibrated using a GRAS 42AA pistonphone calibrator prior to the experiments.

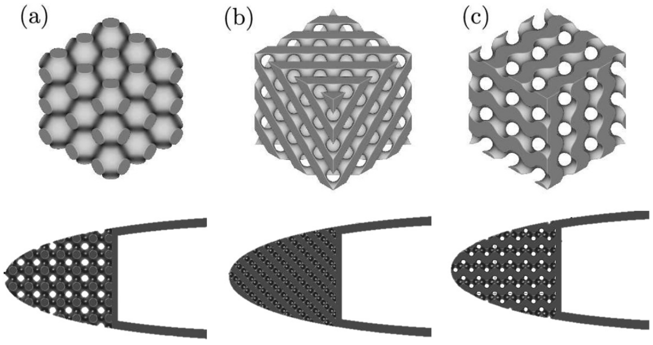

FIG. 3. Triply periodic minimal surface base structures obtained using Eqs. (1)–(3) for (a) Schwarz-P, (b) diamond, and (c) gyroid cases, respectively. The base structures were utilized for the first 10% of the leading edges.

C. Turbulence grids

To generate the incoming turbulence, a set of four grids were placed within the contraction nozzle of the wind tunnel, as shown in Fig. 1. The position of the grids within the tunnel was shown not to affect the normal background jet noise of the wind tunnel,[10] allowing direct noise measurement of the interaction noise between the turbulent flow and NACA 0012 airfoil with various porous leading edges. The geometric properties of the grids and the associated flow properties are outlined in Table I. The integral length scale of the turbulence was estimated by using the autocorrelation method,[53] where the autocorrelation function of the velocity measured by hot-wire anemometry is utilized. The applied method for these calculations is discussed more thoroughly previously.[10]

D. Porous leading edges

As shown in Fig. 2, the first 10% of the leading edge was manufactured to be interchangeable between a solid, instrumented leading edge and the 3D-printed porous leading edges. The chordwise size of the porous leading edge on the airfoil was selected through the previous study which demonstrated that 10% of the chord was the optimum length of chord that maximized noise reduction, while minimizing the amount of chord that would be occupied by the porous structure.[24] Three leading edges of different porous structures were selected to study the effect of the bulk porous structure on the reduction of airfoil turbulence interaction noise. The three selected structures were of the triply periodic minimal surface (TPMS) family, namely, Schwarz-P, diamond, and gyroid (Fig. 3). The three structure types were chosen as they are the simplest forms of the TPMS family and, thus, the easiest to control for porosity. These three TPMS structures are well used in additive manufacturing as surface infill, as well as featuring as bone scaffolds in medical engineering.[54–56] The Schwarz-P structure was first presented by H. A. Schwarz in 1865 (Ref. 57) and is defined as

$$\cos(lx) + \cos(ly) + \cos(lz) = a \tag{1}$$

the diamond structure is also a structure defined by Schwarz in 1865 (Ref. 57) as

TABLE I. The geometric properties of the turbulence grids, and the flow properties at the contraction nozzle exit, $x = 0$, at a freestream velocity $U_\infty = 20$ m/s. The definitions of d and M can be found on Fig. 1.

Name	Diameter, d (mm)	Mesh, M (mm)	σ	Turbulence intensity (%)	Integral length scale (mm)
Grid 1	19	75	0.45	4.8	5.9
Grid 2	19	100	0.35	4.9	6.1
Grid 3	32	167	0.35	8.1	9.4
Grid 4	45	233	0.35	10.1	10.8

TABLE II. Properties of the porous structures used in the design of leading edges.

Structure	Porosity, φ (%)	Minimum pore diameter, d_{pore} (mm)	Permeability, κ
Schwarz-P	50	1.48	3.78×10^{-9}
Diamond	50	0.99	3.96×10^{-9}
Gyroid	50	1.05	4.25×10^{-9}

TABLE III. Boundary layer hot-wire measurement locations around the leading edge, presented in Fig. 13. $x/c = 0$ is the stagnation point on the airfoil and $y/\delta_s = 0$ is the airfoil surface.

x/c	y/δ_s
0.05	0.47
0.10	0.74
0.15	1.00
0.31	1.26

$$\sin(lx)\sin(ly)\sin(lz) + \sin(lx)\cos(ly)\cos(lz) + \cos(lx)\sin(ly)\cos(lz) + \cos(lx)\cos(ly)\sin(lz) = a \quad (2)$$

and the gyroid structure was first published by Schoen[58] and is defined as

$$\cos(lx)\sin(ly) + \cos(ly)\sin(lz) + \sin(lx)\cos(lz) = a, \quad (3)$$

where l is used to define the unit length of the structure and a is used to control the porosity. The porous leading edges were printed using a FormLabs Form3 stereolithography (SLA) printer. The outer shape, surface finish, and size of each produced porous leading edge insert were kept consistent for this experiment. The outer shape and size were controlled through the CAD process, which was performed with a Boolean between the bulk porous structure and verified with a negative mold of the NACA-0012 leading edge profile. A consistent manufacturing process for each porous insert ensured comparable surface finish, confirmed by rigorous post-processing and visual inspection. Further information on the process is detailed in the literature.[49] The tested structures were characterized prior to the tests for both porosity and permeability. The properties of the designed structures are provided in Table II. The porosity and structure of each sample are predefined in the CAD software and verified by the mass of the 3D-printed structure. The airflow permeability of each structure was determined using a permeability test rig. The pressure drop across a cylindrical test sample of each structure was measured, and the airflow permeability was calculated using the Dupuit–Forchheimer equation, $\Delta p/t = \mu/\kappa v_D + \rho C v_D^2$, where C is the form drag coefficient. The permeability is found through the form drag coefficient, which is evaluated by the method proposed by Antohe *et al.*[59] By rearranging the Dupuit–Forchheimer equation, the least mean squared quadratic function can be fitted to the curve of pressure drop as a function of fluid velocity, where the equation of a line is $y = mx + c$, where $m = \rho C$ and $c = \mu/\kappa$. Therefore, the fitting of the line can be utilized to determine m and c, where y is $\frac{\Delta p}{L v_D}$ and x is v_D.

The apparatus for the measurements is shown in Fig. 4. The tube was constructed to be four meters in length and 30 mm in diameter, allowing for the flow to fully develop with in the pipe and allowing the necessary length for the pressure recovery downstream of the sample. The samples were mounted halfway along the tube in a specifically made sample holder. The tube was drilled with multiple holes to facilitate pressure measurement at multiple locations along the tube. The number of pressure taps increases close to the sample section in both the upstream and downstream directions. The airflow to the rig is supplied by a compressed air system to allow for a constant back pressure. The tube is designed with a standard pneumatic fixing connected to an expansion chamber that features flow conditioning. Inline pressure control was facilitated by a regulator and water trap to deliver flow velocities between 2 and 10 m/s. The rig then vents to the atmosphere via a bell mouth to allow for a more gradual pressure change.

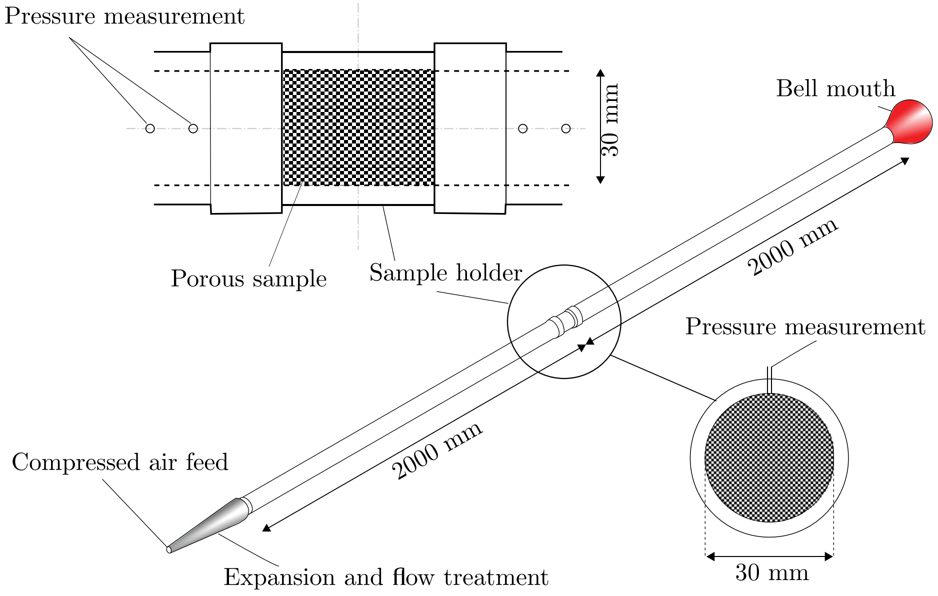

FIG. 4. Permeability test rig schematic.

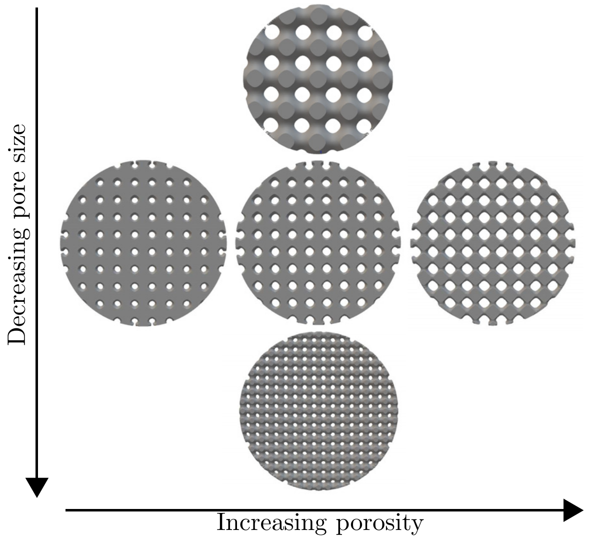

FIG. 5. Permeability rig test samples demonstrating changing in pore size and porosity for a selection of Schwarz-P samples.

A Scanivalve ZOC 22B/32Px pressure scanner was used to measure the pressure from pitot tubes inserted into the computer numerical control machined holes. The pitot tubes were for both static pressure and dynamic pressure measurement along the tube and across the samples. Pressure was sampled at a rate of 500 Hz for 30 s. The total pressure before and after the sample is used to calculate the pressure drop, ΔP. This was conducted for six flow velocities between 2 and 10 m/s in order to gain the gradient of the pressure drop and calculate the static airflow permeability of each sample. The sample length was varied between 5 and 50 mm, and it was found that samples of 10 mm thickness were sufficient to accurately capture the permeability. A total of 110 samples were characterized for pressure drop and subsequent permeability, with varying structure, porosity, and pore size being tested, illustrated by Fig. 5.

Figure 6 presents the relation between porosity and permeability for the matrix of 110 samples. The samples vary in porosity, pore size via the characteristic length and the base structure (Schwarz-Primitive, Gyroid and Diamond). The data are quite revealing in several ways. First, evident from Fig. 6(a) is the porosity and permeability sit on the same curve of the metal foams that were previously tested.[51] However, the porosity of the TPMS samples is generally lower due to the amount of surface area when comparing an open cell foam to the TPMS structure. Second, it is clear from the figure that the permeability porosity relationship causes the results of almost all samples to fall around the same trend line. From Fig. 6(b), it is apparent that although most samples follow the same trend regarding permeability and porosity relationship, variation in permeability for the same porosity is possible. It is clear that there is little, relative change to the value of permeability between a porosity of $0.4 < \varphi < 0.6$. Above a porosity of $\varphi = 0.65$, a small change in porosity can facilitate a large change in permeability. Figure 6(b) highlights where the permeability of each of the leading edge structures lies on the relationship between permeability and porosity.

E. Hot-wire anemometry setup

The flow field upstream of and around the leading edge was characterized by Constant Temperature Anemometry measurements.

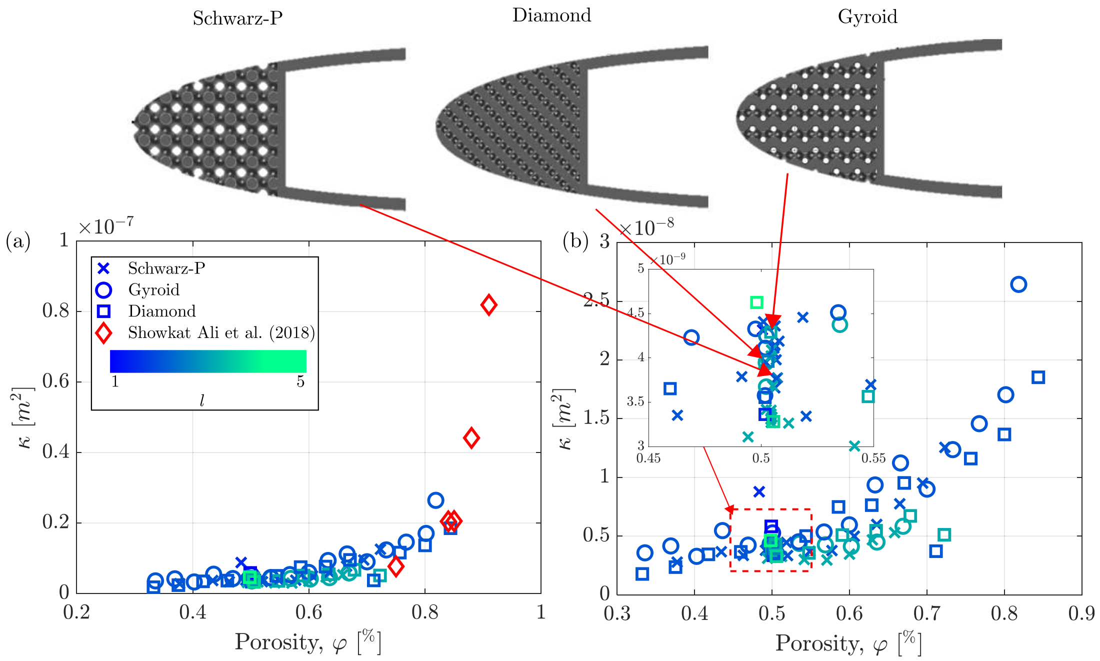

FIG. 6. Permeability and porosity of matrix of 130 test samples of varying structure, pore size, and porosity, where (a) the experimental data are presented with that of Showkat Ali *et al.* and (b) include the location of the porous structures chosen for the leading edges in this study.

The turbulent flow upstream of the airfoil leading edge was measured using a Dantec 55P16 single-wire probe, and the flow around the leading edge of the airfoil was measured with a 55P15 boundary layer probe. A detailed study of the two-point correlation of the velocity fluctuation upstream of the airfoil leading edge was performed using two Dantec 55P16 single-wire probes arranged in tandem configuration, as shown in Fig. 2. All probes were operated using a Dantec Streamline Pro system with a CTA91C10 module with a low-pass filter of 30 kHz. The data were acquired using a National Instruments PXIe-4499 module mounted in a National Instruments PXIe-1026Q chassis. All hot-wire measurements were sampled at a rate of 2^{15} Hz for a duration of 16 s. The velocity data required for two-point correlation studies were sampled simultaneously. All hot-wire probes were calibrated daily using a Dantec 54H10 calibrator. The uncertainty of the velocity measurement was estimated as 2.72% for a free-stream velocity of 20 m/s, with a confidence interval of 95% with reference to the velocity calibration. The uncertainty of the hot-wire measurements was calculated using the detailed procedure of Jørgeson.[60] The hot-wire probes were traversed using two ThorLabs LTS300 300 mm Translation Stages with stepper motor along the x-axis and y-axis with a positioning accuracy of $\pm 5\,\mu$m. The tandem probes were arranged along the z-axis directly upstream of the airfoil leading edge, see Fig. 2(b). The probes were traversed upstream of the airfoil leading edge to acquire measurements at 35 streamwise locations covering the region $-100 < x < -0.03$ mm, corresponding to $-31.51 < x/r < -0.01$, where r is the leading edge radius of the airfoil, see Fig. 2. Two-point correlations for a broad range of separation distances were obtained with traverse measurements with the separation distance ranging between $5.3 < \Delta z < 27$ mm, corresponding to $1.67 < \Delta z/r < 6.40$.

III. RESULTS AND DISCUSSION

The experimental results impart a comprehensive picture of the turbulence interaction phenomenon with a sound understanding of the effect of utilizing a porous leading edge on the flow field and noise generation. The results of the solid leading edge are also provided for all cases to enable a thorough understanding of the effect of the porous leading edges. In Sec. III A, far-field noise characteristics under varying turbulent flows are presented first to study the effect of porous structures. Second, results regarding the spectral and statistical analysis of the velocity fluctuations around and upstream of the leading edge for different leading edge cases are provided. Coherence analysis between the near-field surface pressure fluctuations to far-field pressure fluctuations is presented to realize the link between the airfoil surface pressure and far-field noise. Finally, to complete the analysis, the communication between the velocity fluctuations upstream and the surface pressure fluctuations on the airfoil is studied. All the results presented in this section were obtained for a free stream flow velocity of $U_\infty = 20$ m/s, corresponding to a chord-based Reynolds number of $Re = 2.5 \times 10^5$.

A. Turbulence interaction noise analysis

This section provides far-field noise results for the NACA 0012 airfoil with porous leading edges immersed in varying turbulent flows. The results are presented in comparison with a solid leading edge case. First, we consider the power spectral density (PSD) level of the pressure fluctuations measured by the far-field microphone directly above the leading edge of the airfoil, i.e., $\theta = 90^\circ$, over the frequency range of $160 < f < 10\,000$ Hz. The PSD is calculated as $10 \cdot \log_{10}(\phi_{pp}/p_0^2)$, where ϕ_{pp} is the frequency-dependent energy content of the measured acoustic pressure calculated via Welch's method[61] and p_0 is the reference pressure of 20 μPa. The spectrum was calculated with a block size of 4096 with an overlapping ratio of 50% and a Hamming window. The resulting spectrum had a frequency resolution of $\Delta f = 2$ Hz.

To enable a better interpretation of the PSD results, ΔPSD, i.e., $\Delta PSD = PSD_{solid} - PSD_{porous}$, is also calculated and presented with the corresponding plot. A positive value of ΔPSD denotes a noise reduction, whereas a negative value denotes a noise increase. It is important to note that the measured interaction noise for the solid airfoil is significantly in excess of the normal background noise of the wind tunnel jet between $160 < f < 1000$ Hz. Above $f > 1000$ Hz, the generated airfoil turbulence interaction noise does not exceed the normal background noise of the facility. These observations are previously demonstrated in Bowen *et al.*[10]

Figure 7 shows the turbulence interaction noise spectra for the NACA 0012 airfoil with solid and porous leading edges between $160 < f < 10\,000$ Hz. The far-field noise results are presented for the NACA 0012 airfoil in four different turbulent flows, Figs. 7(a)–7(d), which correspond to the flow generated by grid 1 to grid 4, respectively. Each flow has a varying level of turbulence intensity and integral length scale (see Table I). At first glance, the porous leading edge results demonstrate varying levels of noise reduction. Overall, the PSD results demonstrate the typical behavior of porous materials used to reduce turbulence interaction noise for each presented turbulent flow, i.e., a low-frequency reduction accompanied by a high-frequency increase, which is consistent with the literature.[32,43,44]

The observed frequency range for the noise reduction ($160 < f < 1000$ Hz) and increase ($1000 < f < 10\,000$ Hz) are consistent across the generated turbulent flows. Furthermore, the frequency of the peak noise reduction ($400 < f < 500$ Hz) is also consistent across different inflows, i.e., the flows generated from the four turbulence grids. Considering the PSD results, it is evident that the turbulent flow characteristics, i.e., turbulent length scale and intensity affect the noise reduction performance of the porous leading edge treatment.

The ΔPSD results reveal that the most significant noise reduction the porous leading edges achieve is in the turbulent flow produced by grid 4. Moreover, the increase in turbulence intensity and integral length scale in each flow from grid 1 through grid 4 increases the level of turbulence interaction noise observed. As a result, the effectiveness of the porous leading edges for noise reduction increases with the length scale and turbulence intensity level.

Considering Fig. 7(d) in more detail, the Schwarz-P and the gyroid structure porous leading edges demonstrate comparable PSD results over the presented frequency range with a marked noise reduction of up to 5 dB/Hz at lower frequencies and a noise increase above $f > 2000$ Hz. Furthermore, the diamond structure porous leading edge PSD results demonstrate the lowest level of noise reduction and a comparative noise increase above $f > 2000$ Hz compared to the solid leading edge case results. If one considers the pore size of the porous leading edges structures (see Table II), further insight can be gained between pore size and the turbulent flow. Recall that the porosity was kept constant across the porous structures utilized. The Schwarz-P structure has a larger minimum pore diameter and lower permeability compared to the gyroid structure ($d_{pore,S} = 1.48$ mm and $\kappa_S = 3.78 \times 10^{-9}$). Furthermore, the gyroid and diamond structures

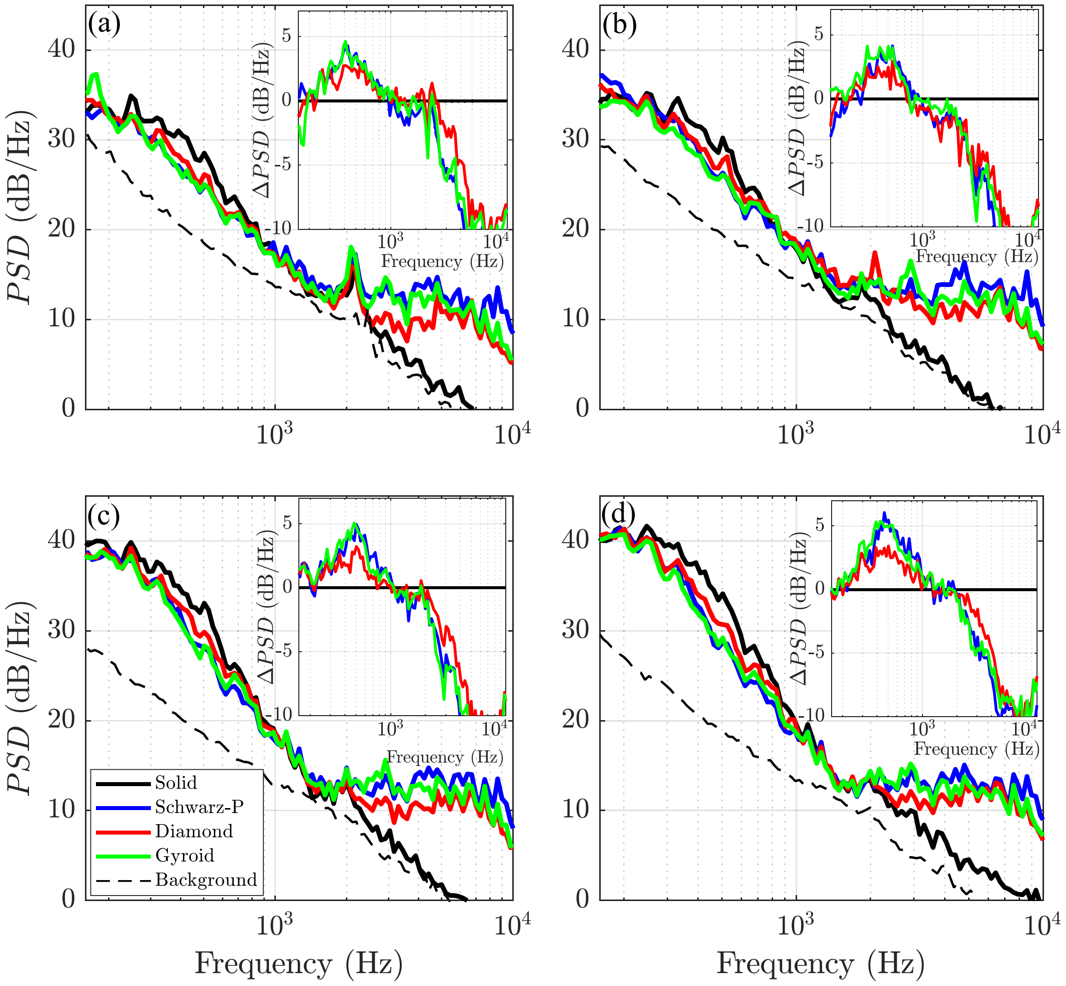

FIG. 7. Far-field noise spectra and associated ΔPSD measured at 90° above the leading edge of the NACA 0012 airfoil with the solid leading edge and Schwarz-P, diamond, and gyroid structure porous leading edges, immersed in the turbulent flow generated by (a) grid 1, (b) grid 2, (c) grid 3, and (d) grid 4.

have comparable minimum pore sizes ($d_{pore,D} = 0.99$ mm and $d_{pore,G} = 1.05$ mm, respectively), whereas the diamond structure has a lower value of permeability ($\kappa_D = 3.96 \times 10^{-9}$ and $\kappa_D = 4.25 \times 10^{-9}$, respectively). Considering the pore size and permeability information together, the PSD results demonstrate that both the permeability and pore size affect the reduction of turbulence interaction noise.

To impart a complete picture of the far-field noise characteristics, the overall sound pressure level (OASPL) of the far-field noise is presented as directivity plots. The overall sound pressure level is calculated as

$$OASPL = 10 \cdot \log_{10}\left[\frac{\int \phi_{pp}(f)df}{p_{ref}^2}\right] \tag{4}$$

integrating the energy spectrum with respect to a frequency between $160 < f < 20\,000$ Hz. The OASPL integration is carried out between 160 and 20 000 Hz to account for the cutoff frequency of the anechoic chamber. Figure 8 presents the directivity of the interaction noise OASPL results with solid and porous leading edges for the flows from the four turbulence grids, and Figs. 8(a)–8(d) display the results of the flow from grids 1–4 (see Table I), respectively. Initial inspection of the results demonstrates that the porous treatment is more effective for an incoming turbulent flow with a larger length scale and higher turbulence intensity. It is clear across the four turbulent flows and three porous types that the noise reduction achieved by the gyroid structure leading edge case outperforms the noise reduction of the Schwarz-P and diamond structure cases. The OASPL results of the gyroid leading edge exceed 3 dB for polar angles between $60° < \theta < 120°$.

It should be noted that when comparing the results of the porous leading edge cases with Schwarz-P and diamond structures in conjunction with the results of the solid leading edge, the diamond structure treatment achieves a further reduction in far-field noise than the Schwarz-P structure treatment for flows with smaller length scales and lower turbulence intensity levels, i.e., cases with grid 1 and grid 2, [see Figs. 7(a) and 7(b)]. However, for flows with larger length scales and

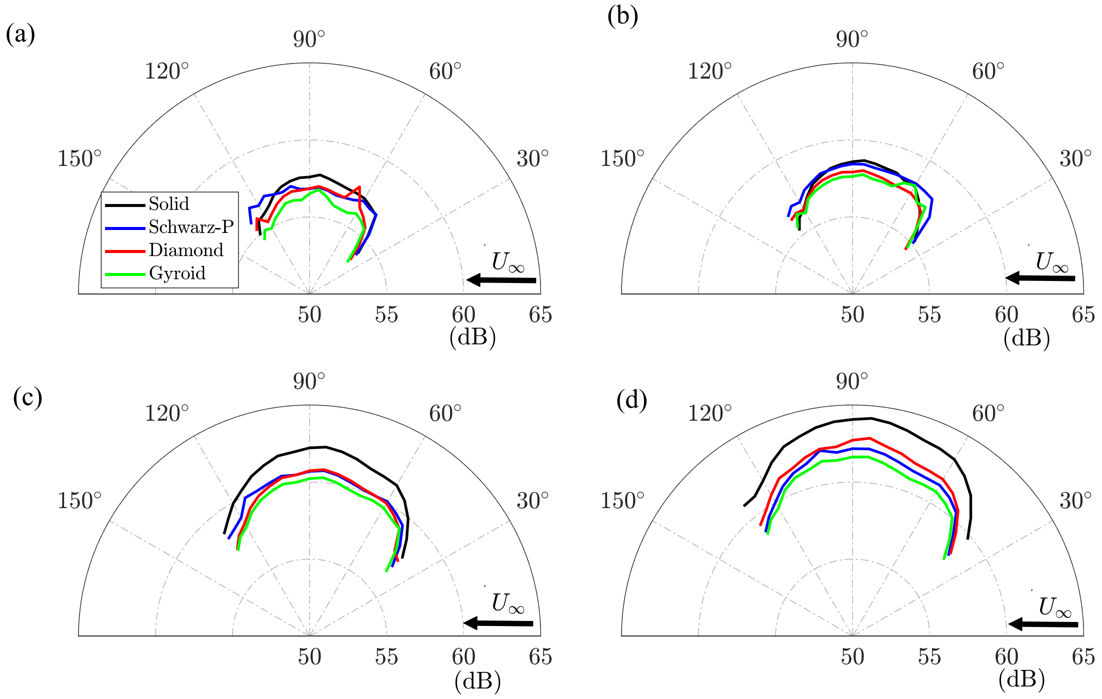

FIG. 8. Directivity of the overall sound pressure level of the airfoil turbulence interaction noise for the NACA 0012 airfoil with the solid and porous leading edges, immersed in the turbulent flow generated by (a) grid 1, (b) grid 2, (c) grid 3, and (d) grid 4.

higher turbulence intensity levels, i.e., cases with grids 3 and grid 4 [see Figs. 7(c) and 7(d)], the Schwarz-P structure leading edge begins to out-perform the diamond structure leading edge for far-field noise reduction. Considering the geometric properties of the porous structures, the diamond structure pore size is smaller than the Schwarz-P structure. When comparing the porous structure size to the turbulence length scale, a correlation can be observed between the noise reduction, the structure pore size, and the integral length scale of the turbulent flow. As the length scale and turbulence intensity level of the flow increases, the larger porous structure size becomes more effective in far-field noise reduction.

It is also worth noting that the treatment of the porous leading edge shows no dramatic change to the noise directivity pattern despite the marked reduction in OASPL. To understand how the porous leading edges achieve noise reduction performance presented in this section, an investigation of how the flow field interacts with leading edges should be carried out. The velocity fluctuations measured upstream of and over the airfoil leading edge are explored in Sec. III B.

B. Turbulent inflow and stagnation

The properties of the turbulent flow and its distortion upstream of the airfoil leading edge are considered to be significant in the generation of turbulence interaction noise.[38,62] The changes to the turbulent flow in the vicinity of the airfoil, caused by the porous leading edges, are investigated by assessing velocity measurements upstream of the stagnation point. Analysis of the mean flow velocity and the velocity fluctuations upstream of the stagnation point reveal information regarding the penetration of the flow into the porous section. To shed light on the nature of the velocity fluctuations in the vicinity of the leading edge, statistical analysis is employed. Spectral analysis is key to understanding the redistribution of energy caused by the introduction of a porous leading edge. Furthermore, two-point spanwise coherence reveals the behavior of the turbulent structures approaching the leading edge and how the porous leading edge influences their behavior. The listed parameters are considered herein to address the observed airfoil turbulence interaction noise reduction in Sec. III A. For brevity, the results presented in the remainder of this manuscript are presented for the turbulent flow generated by grid 4 only, as the porous leading edges in the flow from grid 4 exhibit the most significant reduction in far-field noise.

An important consideration when assessing the presented velocity analysis results is the experimental equipment employed for the measurements. In this study, a single-wire CTA hot-wire probe was utilized for velocity measurements, which can only measure the total velocity. The design and dimensions of x-wire probes do not allow measurements in the proximity of the surface ($x/r < 2$) without significantly disturbing the flow. On the other hand, a single-wire probe can be traversed right to the airfoil surface. Therefore, when considering the calculation of velocity fluctuations, $u = U - \bar{U_\infty}$, removing the mean flow results in a positive value of u where the vector points in the streamwise direction but can have vertical contributions and a negative value of u where the vector is opposite to the streamwise direction but can also have vertical contributions. Therefore, an increase in the velocity fluctuations denotes an increase in the streamwise direction with contributions from vertical components.

1. Velocity stagnation analysis

To explicate any variation to the flow caused by the porous leading edges, velocity measurements in the region in front of the stagnation point are considered. The velocity measurements were performed by traversing a single-wire hot-wire probe immediately in front of the airfoil leading edge up to five leading edge radii upstream, i.e., $-5 < x/r < -0.01$, where r is the airfoil leading edge radius. Figure 9 shows the results of the velocity measurements in the form of normalized freestream velocity U/U_∞, and normalized root mean square (rms) velocity fluctuations $u_{rms}/u_{0,rms}$, where U_∞ and $u_{0,rms}$ are the freestream mean velocity and freestream rms of velocity fluctuations, respectively, measured at the upstream location of $x/r \approx -32$.

As demonstrated by Fig. 9, the flow far upstream of the leading edge, i.e., $x/r > -1.5$, is comparable between the solid and porous leading edge cases for the mean velocity and rms of velocity fluctuation results. The main discrepancies between the results of the solid and porous cases are evident in the proximity of the leading edge, i.e., $-1.5 < x/r < -0.01$. The results of the normalized mean velocity, Fig. 9(a), demonstrate that the solid leading edge causes a velocity stagnation at the leading edge, signified by the reduction of mean velocity up to the closest measurement point. It is worth noting that the diamond and gyroid structure leading edges produce mean velocity results comparable to that of the solid leading edge for the presented spatial extent, $-5 < x/r < -0.01$. In contrast, the results of the Schwarz-P leading edge exhibit a drastically different normalized mean velocity profile, with no significant velocity stagnation in the proximity of the leading edge, i.e., $-1.5 < x/r < -0.01$, indicating the penetration of the flow into the porous leading edge.

Figure 9(b) further highlights the differences between the cases in terms of the root mean square of the velocity fluctuations. For the solid leading edge case, the rms of velocity fluctuation reduces approaching the stagnation point ($-5 < x/r < -0.25$), followed by a sudden increase in close proximity ($-0.25 < x/r < -0.01$) of the leading edge. This is believed to be caused by the redistribution of energy from the streamwise (u) to the crosswise velocity component (v).[62,63] The results of the Schwarz-P leading edge are striking due to the behavior of the rms of velocity fluctuations in the region $-1 < x/r < -0.01$, which demonstrate a sudden marked increase where the results of the other leading edge cases continue to reduce. The Schwarz-P structure pore size is considerably larger than that of the diamond and gyroid structures, and therefore, the solid region of the structure is also larger. It is probable the increase in the velocity fluctuation for Schwarz-P, in some part, is down to flow organization at the point of penetration. Further contribution could come from the pore orientation, as it aligned with the incoming stagnating flow, which will increase the effective flow penetration.

The diamond and gyroid structures present similar velocity rms results between $-5 < x/r < -0.25$ although the reduction in the velocity rms is more significant in the diamond structure case. Furthermore, the results of both the diamond and gyroid structure follow a comparable trend to that of the solid leading edge for $-5 < x/r < -0.25$. The gyroid leading edge exhibits a significant increase in the velocity rms of in the proximity of the leading edge, whereas the recovery is much lower for the diamond structure leading edge. The observations regarding the velocity measurements between porous leading edges are compelling considering their similar noise reduction capabilities yet disparate velocity rms results. The results suggest that despite the comparable permeability and identical porosity, the flow along the stagnation line does not impart the full story for the noise reduction, as previously suggested in the literature.

To gain further insight into the influence of the porous leading edges on the airfoil–turbulence interaction, statistical investigation of the velocity fluctuations in the region approaching the stagnation is performed through skewness $S(u)$ and kurtosis $K(u)$ analysis. The skewness value gives insight into the shape of the probability density function (PDF) of velocity fluctuations distribution, and the kurtosis value sheds light on the shape and tails of the distribution.[64] A skewness value of $S(u) = 0$ indicates a symmetric distribution, and positive

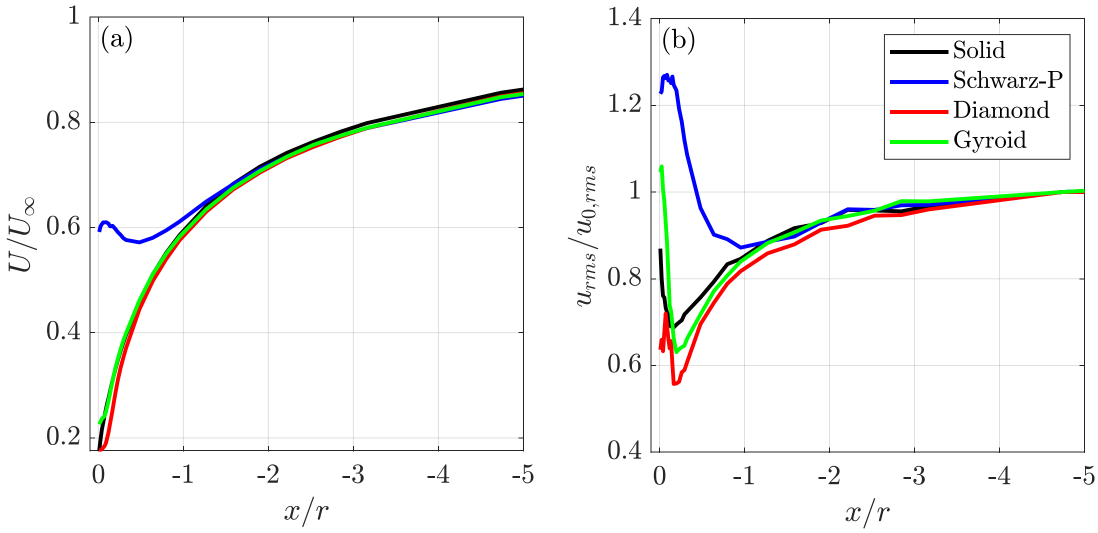

FIG. 9. Comparison of velocity measurement results for the solid and porous leading edges along the stagnation streamline in the flow generated by grid 4, (a) normalized flow velocity (U/U_∞) and (b) normalized rms of velocity fluctuation $u_{rms}/u_{0,rms}$.

and negative values of skewness represent skewed velocity fluctuations in a positive and negative direction, respectively. The Gaussian distribution of velocity fluctuation is denoted by $K(u) = 3$, whereas $K(u) < 3$ denotes a lightly tailed distribution and $K(u) > 3$ denotes a heavily tailed distribution.[64]

Figure 10 presents the skewness and kurtosis of the velocity fluctuations upstream of the airfoil leading edge for the region $-5 < x/r < -0.01$ for all cases. The skewness results for all the leading edge cases are comparable and represent freely decaying turbulence for the region $-5 < x/r < -0.5$. Similarly, the kurtosis results at the region upstream of the leading edge are comparable for all cases. However, for the kurtosis results, the variation between the cases emerges further upstream of the leading edge, i.e., $x/r \approx -1.5$. In the vicinity of the leading edge, $-0.5 < x/r < -0.01$, the solid leading edge results exhibit a significant, positive skewness denoting an increase in the positive velocity fluctuations distribution, evident for the same x/r region of the velocity fluctuation recovery in the velocity fluctuation (Fig. 9). The kurtosis value for the solid leading edge begins to deviate from $K(u) = 3$ within $x/r < -1.5$, approaching the leading edge, and rapidly peaks to a maximum value of $K(u) = 4.6$ in front of the stagnation point. Interpretation of the skewness and kurtosis results for the solid leading edge indicates an increase in the positive velocity fluctuations (skewness) coupled with an increase in the regularity of the strongest fluctuations (kurtosis).[65] The skewness results of all three porous leading edges demonstrate no significant deviation from $S(u) \approx 0$, indicating that the porous structure notably manipulates the statistical behavior of the velocity fluctuations at the leading edge compared with the solid leading edge. The kurtosis results for the porous leading edges show comparable results to the solid leading edge for over $-5 < x/r < -1.5$. Furthermore, both the gyroid and diamond leading edge case results to exhibit similar behavior, which follows a similar trend to the solid case up to $x/r \approx -0.2$, except for the rapid increase in the proximity of the leading edge. On the other hand, the Schwarz-P case results demonstrate a decrease in the kurtosis value, i.e., the exact opposite behavior to the other two porous cases, within $x/r < -1$.

Based on the skewness and kurtosis results, it is apparent that the porous leading edges significantly affect the statistics of the velocity fluctuations in close proximity to the airfoil leading edge. As each of the three leading edge structures exhibits a significant reduction in the skewness and kurtosis compared with the solid leading edge results, it can be suggested that changes to the PDF of the velocity fluctuations due to the porous leading edges are, in part, responsible for the reduction of the turbulence interaction noise. Furthermore, the similarity of the results for diamond and gyroid-based leading edges displayed in Fig. 10 indicates that the distortion experienced by the velocity fluctuations does not impart the full picture of the changes to the flow in the vicinity of a porous leading edge. The results of the statistical analysis suggest that the porous leading edges influence the distribution of the velocity fluctuations, changing the behavior of the turbulent flow in the vicinity of the leading edge. The reduction in the change in skewness and kurtosis is an indicator of the noise reduction generated by the porous leading edges; however, the energy content of the velocity fluctuations must be assessed to shed further light.

The spectral characteristics of the velocity fluctuations at the upstream of the velocity stagnation are presented to understand the frequency-energy content in the form of the power spectrum (ϕ_{uu}), estimated using the Welch method.[61] The power spectral density results (PSD) of the velocity fluctuations are presented as the pre-multiplied energy spectra. This presentation of the ϕ_{uu} data aids in the interpretation of energy change between measurement locations and between cases. The pre-multiplied energy spectra are calculated as, $f\phi_{uu}/u_{0,rms}^2$), where $u_{0,rms}$ is the rms velocity fluctuation of the freestream measured at $x/r \approx -32$.

Figure 11 presents the pre-multiplied energy spectra of the velocity fluctuations upstream of the leading edge of the NACA 0012 airfoil for each leading edge treatment, namely, solid, Schwarz-P, diamond, and gyroid structure. The pre-multiplied energy spectra of the velocity fluctuations for the solid leading edge, from the freestream location $x/r = -32$–-0.15, demonstrate a reduction in the energy levels coupled with the peak pre-multiplied energy moving to higher frequencies.

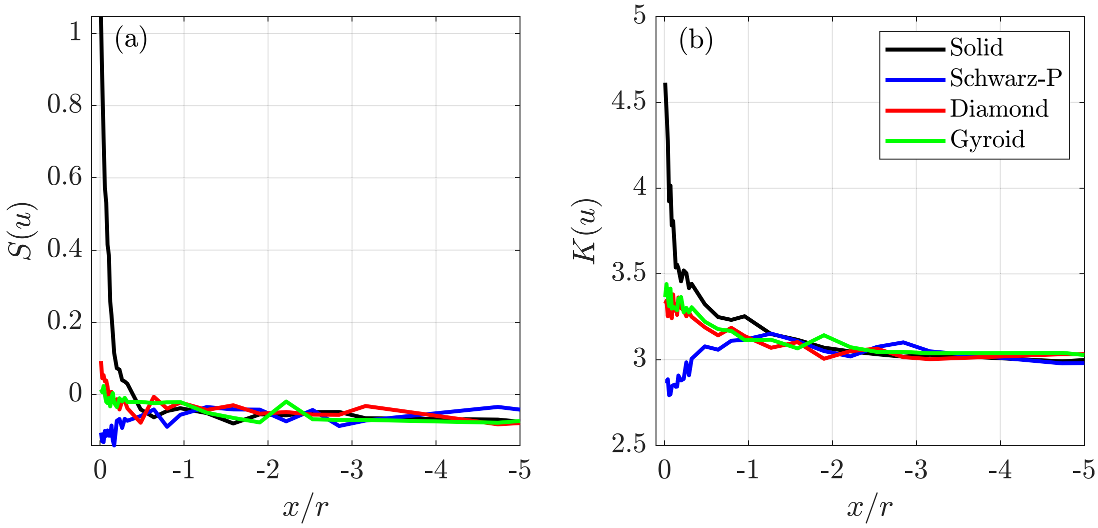

FIG. 10. Comparison of (a) skewness $S(u)$ and (b) kurtosis $K(u)$ of the velocity fluctuations along the stagnation streamline for the NACA 0012 with solid and porous leading edges.

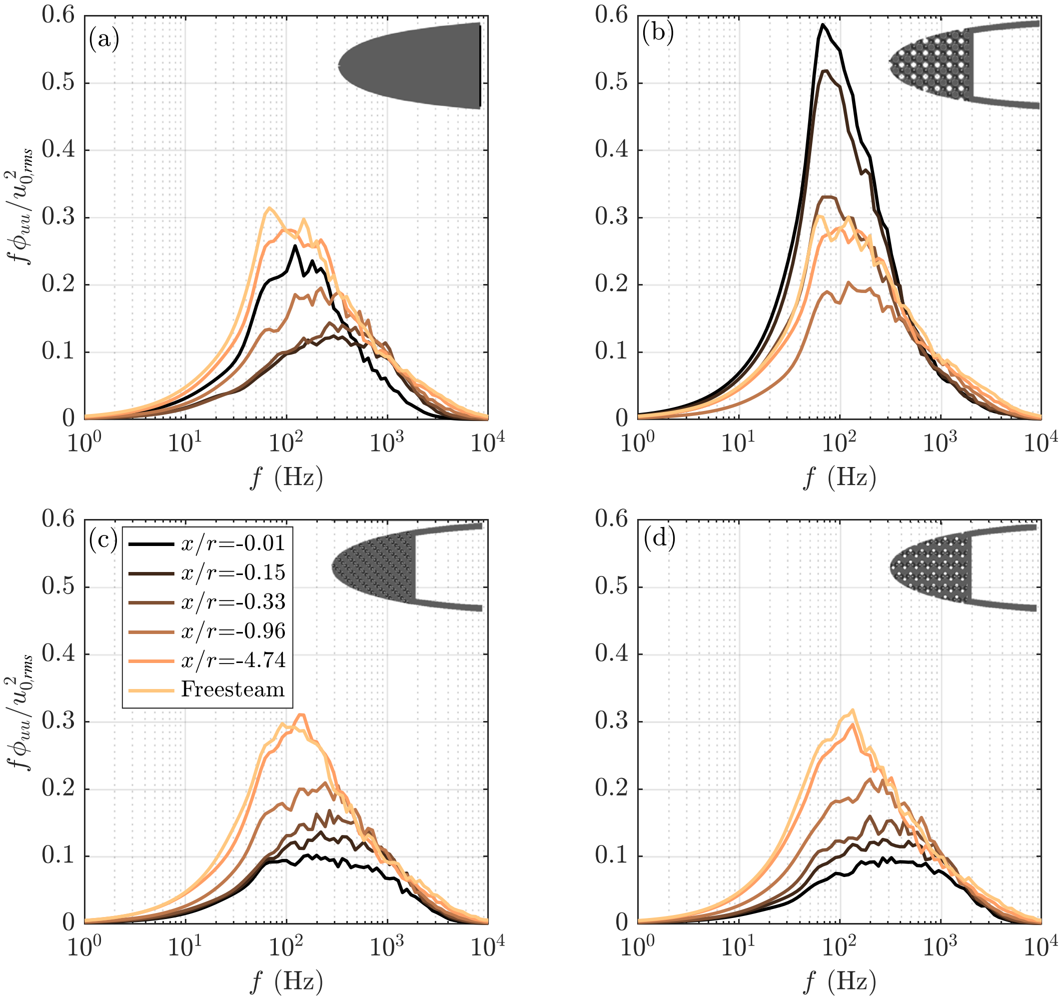

FIG. 11. Pre-multiplied energy spectra of the velocity fluctuations along the stagnation streamline upstream between $-4.74 < x/r < -0.01$ of the NACA 0012 airfoil for (a) solid leading edge and porous leading edges (b) Schwarz-P structure, (c) diamond structure, and (d) gyroid structure.

At the stagnation point, $x/r = -0.01$, there is some recovery of the velocity fluctuation energy level, yet it remains lower than that of the freestream flow result ($x/r = -32$). Comparing the results of the solid leading edge and the three porous leading edge cases, it is evident that the velocity fluctuation energy spectra are similar for all cases from the freestream point ($x/r \approx -32$) approaching $x/r = -0.96$. In closer proximity to the Schwarz-P leading edge, between $-0.15 < x/r < -0.01$, there is a rapid increase in the energy of the velocity fluctuations, in corroboration with the elevated rms of the velocity fluctuations evident in Fig. 9(b). The increase in energy, which is centered at $f = 70$ Hz, exhibits the most energetic turbulence scales between $40 < f < 300$ Hz. This is a direct consequence of the flow into and around the porous media, which is coupled with an increase in spanwise coherence of velocity fluctuation, as previously shown.[45]

The pre-multiplied energy spectra results for the diamond and gyroid leading edge structures are vastly different to the results of both the solid case and the Schwarz-P case within $-0.33 < x/r < -0.01$, where the results exhibit a further decrease in the energy level in front of the stagnation point. The results of the diamond and gyroid cases differ at $x/r = -0.01$, highlighted by the broadband hump reduction between $40 < f < 300$ Hz for the gyroid leading edge case compared to the results of the diamond leading edge results.

2. Two-point correlation analysis

The two-point correlation of the velocity fluctuations along the stagnation line, schematically illustrated in Fig. 2, offers valuable information on the level of coherence of the flow structures and their physical size in the spanwise direction. By performing several two-probe coherence studies at different streamwise locations upstream of the leading edge, one can study the changes to the size of the turbulent flow structures as they approach the airfoil leading edge. The magnitude-squared of the spanwise coherence is calculated as

$$\gamma^2_{u_iu_j}(f,\Delta z) = \frac{\phi_{u_iu_j}(f)^2}{\phi_{u_iu_i}(f)\phi_{u_ju_j}(f)}, \qquad (5)$$

where $\gamma^2_{u_i'u_j'}(f, \Delta z)$ is the spanwise coherence calculated between two single-wire probes in a tandem configuration, separated by Δz, and $\phi_{u_i'u_j'}$ denotes the cross-power spectral density between the two probes i and j, respectively. Figure 12 presents the results of the spanwise coherence of the velocity fluctuations for the flow upstream of the stagnation point at four locations (freestream, i.e., $x/r = -33$, and $x/r = -0.96$, -0.33, and -0.01) for the solid leading edge, and three porous structure leading edges, i.e., Schwarz-P, diamond, and gyroid.

In corroboration with earlier results, at the freestream (i.e., $x/r = -33$) and $x/r = -0.96$ locations, the spanwise coherence of the velocity fluctuations is comparable for all the leading edge cases. Specifically, there is a high level of coherence at lower frequencies ($f < 1000$ Hz), which corresponds to the frequency range with significant turbulence interaction noise as observed in the far-field results (Fig. 7). In addition, the results demonstrate a strong dependency on spanwise separation $\Delta z/r$, signified by the reduction in coherence

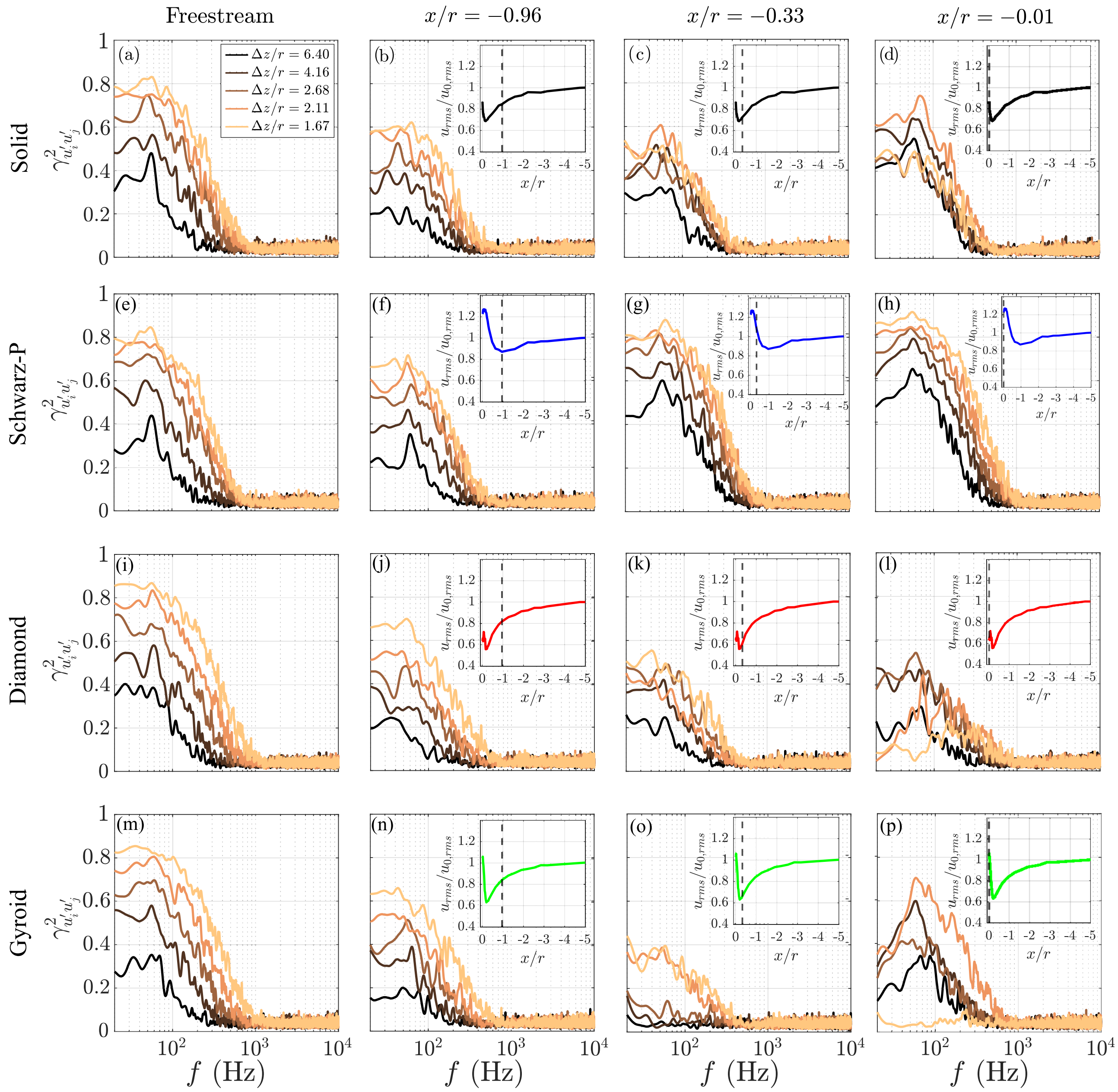

FIG. 12. Spanwise magnitude-square coherence ($\gamma^2_{u_iu_j}$) of velocity fluctuations measured by tandem hot-wire probes at multiple spanwise separations ($\Delta z/r$) at four locations; the freestream at $x/r \approx -32$, and $x/r = -0.96$, -0.33, and $x/r = -0.01$ with (a)–(d) solid, (e)–(h) Schwarz-P structure, (i)–(l) diamond structure, and (m)–(p) gyroid structure leading edge case.

magnitude with the increased value of $\Delta z/r$. On the other hand, the coherence results at high frequencies ($f > 1000\,\text{Hz}$) are found to be weak for all leading edge cases.

Moving closer to the velocity stagnation point, at $x/r = -0.33$, the behavior of the spanwise coherence between the cases begins to deviate significantly among cases. For the solid leading edge, Fig. 12(c), a moderate level of coherence remains for all spanwise separations, which does not change significantly among different $\Delta z/r$ results, signifying the distortion of the turbulent structures in more two-dimensional vortical structures. On the contrary, the Schwarz-P case results demonstrate elevated spanwise coherence levels at this location, including significant variation with respect to the separation distance. Furthermore, when considered with the results of Figs. 9–11, it is clear that the increased energy and coherence are associated with flow organization at the point of penetration, as demonstrated previously.[45] In contrast to the Schwarz-P case, there appears to be a significant reduction in the coherence level for the gyroid and diamond cases at this point, especially at larger spanwise separations. Furthermore, for spanwise separations above $\Delta z/r > 2.68$, there appears to be no observed significant coherence for the gyroid leading edge case. The reduction in the spanwise coherence for the gyroid and diamond leading edge cases signifies a reduction in the size of the vortical structures as they approach the porous leading edge. At the measurement location closest to the leading edge, $x/r = -0.01$, the solid leading edge results exhibit an increase in the spanwise coherence, yet a loss of spanwise sensitivity signified by comparable levels of coherence for every separation distance, further indicating the presence of a two-dimensional vortical structure, a consequence of upwash of the velocity at the stagnation point.

The results of the Schwarz-P case also demonstrate an increase in the spanwise coherence at this location; however, some sensitivity to the spanwise coherence level is retained. The elevated coherence levels may be due to the re-organization of the flow, i.e., a combination of upwash and flow penetration into the porous structure evident in Fig. 9. The results of the diamond leading edge at this location exhibit comparable spanwise coherence to the measurement location $x/r = -0.33$; however, there is a reduction in the coherence level for spanwise separations of $\Delta z/r = 1.67$ and 2.11, denoting a loss in the spanwise sensitivity of the coherence. The results of the gyroid leading edge for $x/r = -0.01$ present an increase in the coherence level compared with the same measurement at $x/r = -0.33$. Furthermore, the broadband hump at $f = 60\,\text{Hz}$, evident in the results of the solid leading edge case at $x/r = -0.33$, manifest in the coherence results of the gyroid leading edge for most spanwise separations. Interestingly, there appears to be a lack of spanwise sensitivity in relation to the coherence level, as there is no coherence observed for the closest spanwise separation of $\Delta z/r = 1.67$.

To summarize, the solid leading edge demonstrates distortion of the vortical structures, increasing the two-dimensionality of the structures approaching the leading edge. The Schwarz-P case displays an increase in coherence approaching the leading edge, which mirrors the increase in rms of velocity fluctuation caused by the re-organization of flow due to larger pore sizes and penetration into the porous structure. The diamond and gyroid structure porous leading edges demonstrate a reduction in the spanwise structure size approaching the leading edge, coupled with a reduction in velocity fluctuation energy. This observation is likely due to flow re-organization at the point of penetration into porous media, causing a reduction of the upwash component evident in the solid leading edge case. These findings suggest a complex nature in the interaction of the flow with a porous leading edge that extends beyond the flow along the stagnation line. All three leading edges demonstrate noise reduction in Fig. 7 and yet exhibit contrasting behavior in the spanwise coherence of the velocity fluctuations approaching the leading edge. These results suggest that further analysis of the flow around the porous leading edge is required to fully understand the noise reduction.

C. Near-surface analysis

The unsteady surface pressure fluctuations on an airfoil in turbulent flow are responsible, in part, for the noise radiated to the far-field.[1] To explore the effect of the porous leading edges on the near-field characteristics of the airfoil response, information regarding surface pressure fluctuations over the porous treatment is required. However, instrumenting leading edges based on small-scale porous structures in a non-intrusive way is a challenging task. Therefore, details about the surface pressure fluctuations over the porous part of the airfoil are difficult to obtain. In an effort to understand the spectral content of the flow field in this region, near-surface velocity measurements were made with a single-wire boundary layer hot-wire probe. Detailed boundary layer measurements were conducted perpendicular to the local airfoil surface at four chordwise locations. Furthermore, measurements were taken at six chordwise locations at a perpendicular distance of less than one leading edge radius from the airfoil surface. The two sets of measurements enabled studying the effect of porous treatment on the changes in the energy spectra both inside and outside the boundary layer.

Boundary layer measurements were used to characterize the boundary layer height of the flow for the solid airfoil, δ_s, from the mean velocity profile at multiple chordwise locations. The boundary layer thickness is found from the point where the flow velocity becomes asymptotic to the freestream, defined as the 99% boundary layer thickness. The definition of the $0.99 \cdot U_\infty$ for an airfoil is based on the curve fitting method of Sagrado (Table III).[48] Four positions in the boundary layer were selected to assess the energy content of the velocity fluctuations close to the airfoil surface and presented as the pre-multiplied energy spectra in Fig. 13. Four chordwise positions were selected to assess the energy in the boundary layer as it develops over and beyond the porous treatments in comparison with the solid airfoil, namely, $x/c = 0.05$, 0.1, 0.15, and 0.31. The selected boundary layer positions were $y/\delta_s = 0.47$, 0.74, 1, and 1.26, and each figure presents the results for the solid leading edge and three porous structures.

Inspection of the results presented in Fig. 13 reveals the significant influence of the porous treatment on the velocity fluctuation energy within the boundary layer, marked by the increase in the energy compared with the solid airfoil results. Furthermore, it can be seen that the permeability and pore size of the porous structure influences the behavior of the velocity fluctuation energy due to the significant rise in the results of the diamond structure leading edge. A distinct double-peak behavior is evident in the energy spectra of all the porous cases, with a significantly higher energy levels for the diamond structure case. On the other hand, for the solid leading edge case, the energy spectra have a single, narrower broadband hump over the presented frequency range. The first peak ($f \approx 70\,\text{Hz}$) in the results of the

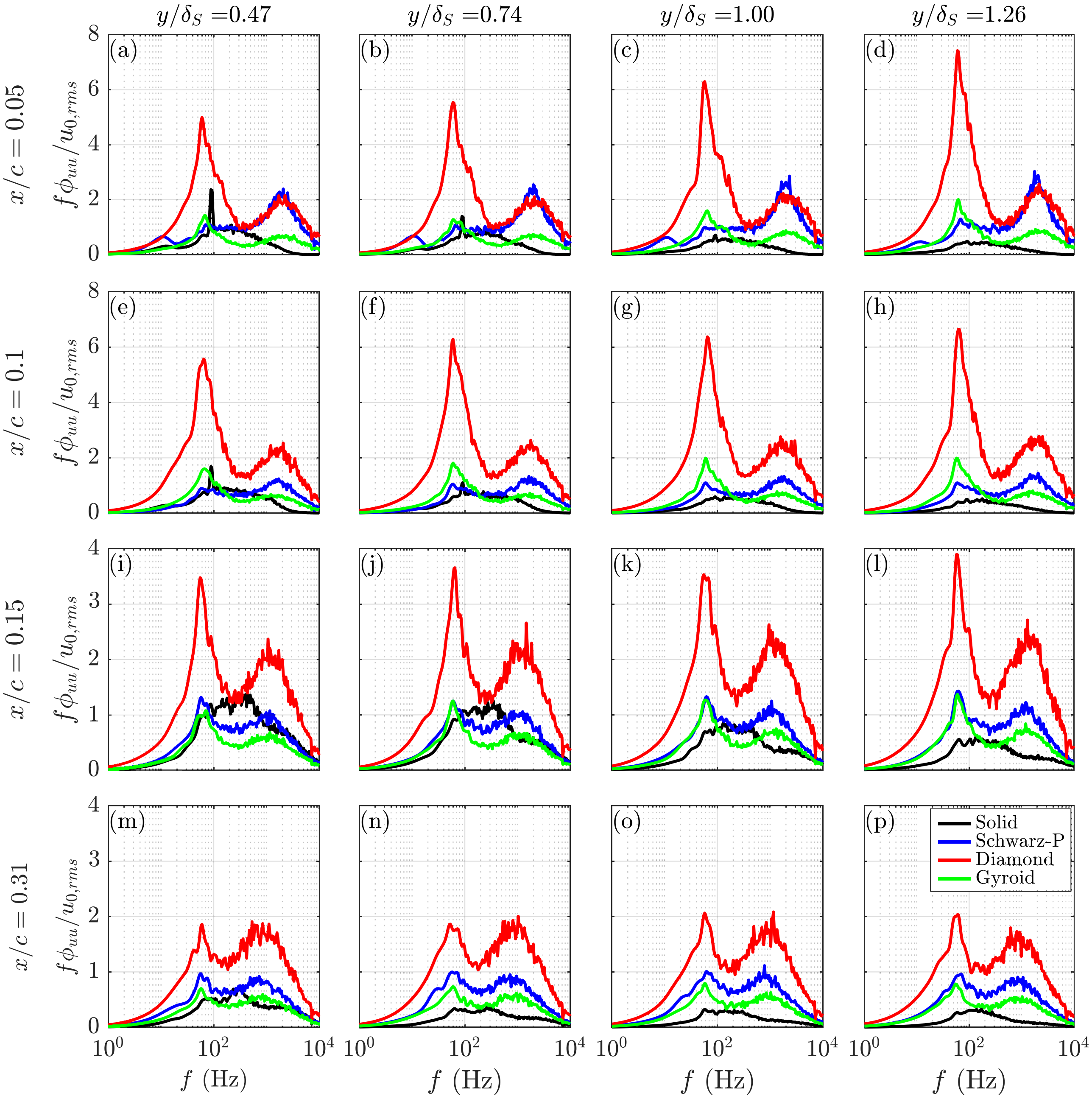

FIG. 13. Comparison of pre-multiplied energy spectra of the velocity fluctuations for near-surface measurements of the NACA 0012 airfoil with the solid leading edge and porous leading edges where [(a)–(d)] are the results at location $x/c = 0.05$, [(e)–(g)] are the results at location $x/c = 0.1$, [(i)–(l)] are results at location $x/c = 0, 15$, and [(m)–(p)] are results at location $x/c = 0.31$, and each column represents a different boundary layer height between $y/\delta_s = 0.47$ and $y/\delta_s = 1.26$.

diamond structure treatment is sensitive to both the location within the boundary layer and chordwise location downstream, as it tends to increase moving away from the airfoil surface (moving from left to right for any *x*/*c* position), yet reduce with the downstream position (moving from top to bottom for any y/δ_s position). The behavior of the first peak is comparable with Schwarz-P and gyroid porous structure results, albeit with a significantly reduced magnitude. In addition, among three porous cases, the lowest energy levels were observed for the gyroid leading edge case. It should be noted that the first peak is centered around the same frequency observed in the two-point coherence results in the proximity of the leading edge, Fig. 12, and could be associated with the hydrodynamic penetration of the flow.

The second peak ($f \approx 1000$ Hz) observed at higher frequencies is initially comparable between the diamond and Schwarz-P leading edge

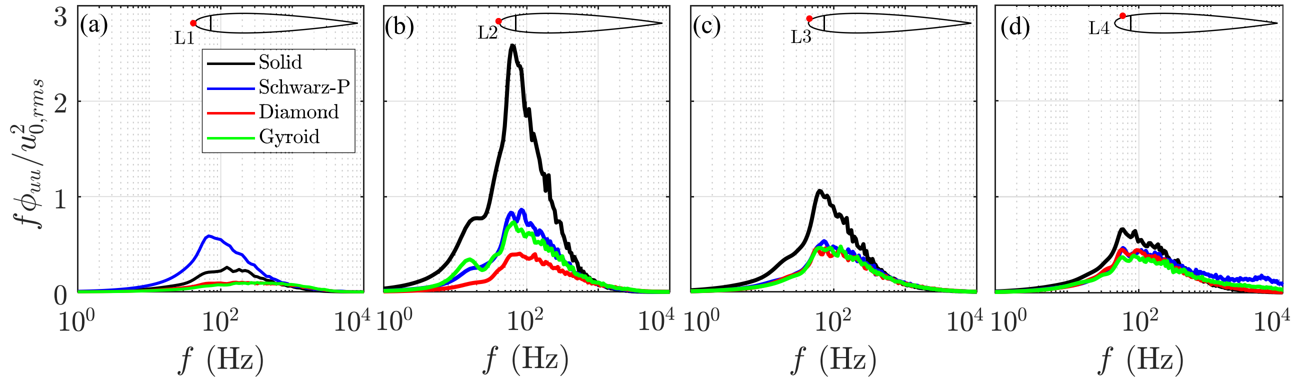

FIG. 14. Comparison of pre-multiplied energy spectra of the velocity fluctuations for near-surface measurements of the NACA 0012 airfoil with the solid leading edge and porous leading edges where the corresponding chordwise positions for [(a)–(d)] described in Table IV for L1–L4.

treatments. The results show little sensitivity to position in the boundary layer at $x/c = 0.05$. As the flow develops downstream, the high-frequency energy levels of the velocity fluctuation over the diamond structure case remain consistent for each chordwise location. However, the high-frequency energy of the Schwarz-P results reduces at $x/c = 0.1$ and remains consistent at locations $x/c = 0.15$ and 0.31. The velocity fluctuation energy results of the gyroid structure at higher frequencies demonstrate comparable energy levels for each location in the boundary layer and each chordwise position.

The double-peak behavior observed in the case of the porous leading edges is indicative of the existence of two different mechanisms, namely, a strong hydrodynamic field generated around and within the porous material with a dominant low-frequency energy content $f \approx 70$ Hz, as previously suggested by Showkat Ali *et al.*,[18] and frictional forces with a peak observed at higher frequencies. As can be observed from the results, the first peak is more dominant near the leading edge and over the porous sample, and its amplitude reduces as we move into the solid position of the airfoil ($x/c > 0.1$). It would appear that the porous structure with the smallest pore size (diamond, $d_{pore} = 0.99$ mm) causes the most dramatic increase in the low-frequency energy. A surprising result considering the diamond structure has the smallest pore size; however, considering the main pore orientation is at an angle of $\pm 45°$ to the flow penetration and re-injection in the region over the leading edge is likely to have a greater effect compared with the gyroid and Schwarz-P structures as the pores are oriented at $90°$ to the flow. This result corroborates with the findings in Fig. 11, where an increase in the velocity fluctuation for the Schwarz-P structure is observed but not for the diamond and gyroid structures. Upstream of the leading edge of the pores are aligned at $0°$ to the flow for the Schwarz-P structure.

The increase in the high-frequency energy content observed for the porous leading edge treatments could be linked to the increase in the high-frequency noise observed at the far-field. Although roughness noise is primarily observed in the far-field and strongly linked to the surface pressure fluctuations, the noise is a result of a scattering mechanism in the boundary layer flow.[66] It is clear that the porous leading edges cause an increase in the high-frequency energy content of velocity fluctuations close to the airfoil surface. The increase in the velocity fluctuation energy spectra could be caused by a combination of the roughness effects in the boundary layer[19] and re-injection of the flow from inside the porous structure at the material impedance jump. This observation suggests that although the porous leading edge treatments generate roughness noise, the perceived level at the far-field is exacerbated by the re-injection of the flow inside the porous structure.

Following the results of the velocity fluctuation energy levels inside the boundary layer, the velocity fluctuation energy levels outside the boundary layer ($y/\delta_s > 10$) and near the airfoil surface at the leading edge are assessed. The pre-multiplied energy spectra of the near-surface velocities measured at four locations spanning the leading edge region for each case are presented through Figs. 14(a)–14(d). The spatial description of the measurement locations is presented in Table IV. In front of the stagnation point, i.e., L1, the energy content of the solid leading edge case is significantly lower than all other measurement locations. At L2, the energy content of the solid leading edge results dramatically increases, which may arise from the velocity acceleration around the leading edge of the airfoil. Spectra results demonstrate a reduction in the low-frequency energy content moving from L3 to L4. The broadband hump peak at $f = 70$ Hz is evident at L2, L3, and L4, consistent with the observations in Figs. 11 and 12. Further downstream at L3, there is a reduction in the low-frequency content and an increase in the high-frequency content of the energy spectra. The reduction of the low-frequency energy content persists for the remaining measurement location, L4, with no significant change to the high-frequency energy content.

The results for porous leading edge cases demonstrate some significant changes in the energy spectra of the velocity fluctuation for the same region. At L1, the stagnation point, Fig. 14(a), the Schwarz-P exhibits significantly higher energy levels of velocity fluctuation than the solid and other porous cases. Both the diamond and gyroid leading edge case results show a reduced level of energy across all frequencies when compared with the solid case. Figure 14(b) demonstrates the

TABLE IV. Hot-wire measurement locations around the leading edge, presented in Fig. 14. $x/c = 0 y/c = 0$ is the stagnation point on the airfoil.

	L1	L2	L3	L4
x/c	–0.01	–0.005	0.008	0.047
y/c	0	0.009	0.03	0.045

significant change in the velocity fluctuation results for a small spatial movement in the y direction. At both L2 ($x/c = -0.005 y/c = 0.009$) and L3 ($x/c = -0.008 y/c = 0.03$), there is a reduction in energy content for all porous leading edge cases when compared with the results of the solid case. The results of Figs. 14(b) and 14(c) demonstrate that a reduction in velocity fluctuation might not be evident at the stagnation point [see Figs. 14(a) and 11(b)]; however, an apparent reduction in the low-frequency energy of the velocity fluctuation is evident over the surface of the porous leading edges. The reduction in velocity fluctuation for the porous cases is still evident at L3 and L4 [Figs. 14(c) and 14(d)] although the magnitude of reduction compared to the solid case has decreased. The results of all three porous leading edges demonstrate a comparable level of reduction to the low-frequency energy compared with the solid leading edge results.

Figure 14(c), which is further along the porous section (i.e., $x/c = 0.008 y/c = 0.03$), demonstrates less reduction of the energy at low frequencies. Furthermore, there is a slight increase in high-frequency energy for Schwarz-P and gyroid cases. Moving to halfway along the porous section to L4 ($x/c = 0.047 y/c = 0.045$), the Schwarz-P and gyroid case results demonstrate comparable results, with a reduction of energy level at low frequencies compared with the solid case.

Near-field analysis of the velocity fluctuation demonstrates pronounced differences between the flow inside and outside the boundary layer. For positions inside the boundary layer, it is clear that porous treatments cause a significant increase in the velocity fluctuation energy compared to the solid leading edge case while developing a double-peak behavior, which does not exist for the solid case. In contrast, the measurements outside the boundary layer demonstrate a marked reduction of the velocity fluctuation energy for the porous leading edges when the solid leading edge exhibits a large increase. The increase in the velocity fluctuation for the solid leading edge is the redistribution of energy from the streamwise to crosswise velocity component due to the flow turning over the airfoil leading edge. Although the velocity fluctuation energy is not a direct cause of the noise reduction, evidence indicates that a reduction in the energy of the velocity fluctuation coincides with the frequency range of the noise reduction at the far-field (Fig. 7). Furthermore, as previously mentioned, the increase in the energy in the boundary layer can be attributed to the far-field noise increase at higher frequencies.[19,66]

D. Pressure–velocity coherence

The influence of the velocity fluctuations upstream of the airfoil leading edge has consequences in the airfoil response over the surface of the airfoil, felt up to 80% of the chord downstream of the leading edge.[67]

The pressure–velocity coherence (p–u coherence) analyses may help us to relate the unsteady surface pressure fluctuations to flow field characteristics over the airfoil. Moreover, p–u coherence may also provide additional insight to characterize the spatial and temporal evolution of the coherent structures of the turbulent inflow and how they interact with the airfoil body. A single-wire hot-wire probe was utilized for velocity fluctuation measurement along the stagnation line between $-4.74 < x/r < -0.01$, while the pressure fluctuations were simultaneously sampled for all transducers on the airfoil. The coherence between the pressure and the velocity signals is calculated as

$$\gamma^2_{p_i u_j}(f, \Delta x) = \frac{\phi_{p_i u_j}(f)^2}{\phi_{p_i p_i}(f)\phi_{u_j u_j}(f)}, \tag{6}$$

where $\phi_{p_i u_j}(f)$ denotes the cross-power spectral density function calculated between the velocity and pressure signals and Δx is the distance between the single-wire probe and the pressure transducer on the airfoil located at x_i and x_j, respectively. Figure 16 presents the $p - u$ coherence between velocity fluctuations measured at two locations in the flow, i.e., $x/r = -4.74$ (upstream location) and –0.01 (stagnation point), to the unsteady surface pressure fluctuations measured on the surface of the airfoil for the solid and the Schwarz-P porous leading edge. As there is no observed pressure velocity coherence for all the porous cases, the gyroid and diamond cases are omitted for brevity. It is worth noting that due to a lack of instrumentation over the porous treatments, the $p - u$ coherence results for the associated cases lack information over $0 < x/c < 0.2$, which is shown as a gray-shaded region [Figs. 15(b) and 15(d)]. Pressure–velocity coherence results calculated with respect to the upstream velocity measurement location $x/r = -4.74$ demonstrate a noticeable relation to pressure fluctuations at the stagnation point, i.e., $x/c = 0$, across a broad range of frequencies for the solid leading edge case. Furthermore, a secondary but slightly weaker coherence island is evident for $0.05 < x/c < 0.2$ at low-to-mid frequencies. Moreover, the substantially elevated $p - u$ coherence levels between the velocity measurements upstream of the stagnation point ($x/r = -0.01$) to the pressure fluctuations over the surface of the airfoil are evident. This observation supports the evidence for the formation of a large two-dimensional coherence upstream of the leading edge, as shown in Fig. 11(d). Comparing the pressure velocity coherence results with the Schwarz-P leading edge case, it is very clear the porous leading edge completely kills the coherence for the porous cases and both velocity measurement locations over the region $0.2 < x/c < 1$. The dramatic reduction of the pressure velocity coherence demonstrates that the turbulent velocity fluctuations just in front of the leading edge have less influence on the unsteady response of the airfoil unlike in the solid leading edge case where a strong coherence is evident. Moreover, the formation of three-dimensional structures in the porous case in front of the stagnation point [see Fig. 11(d)] does not demonstrate any coherence to the pressure fluctuations on the surface of the airfoil. It is clear that the velocity fluctuations in front of the leading edge communicate with the surface pressure over a significant portion of the airfoil surface. As the surface pressure response of the airfoil is responsible for the noise propagated to the far-field,[1] the dramatic reduction in the pressure–velocity coherence for the porous leading edges could be attributed to the reduction of the far-field noise.

E. Near-field to far-field coherence

Over the course of the presented results, it has been made clear that the far-field noise is reduced by utilizing a porous leading edge. The spectral and statistical velocity analysis hints at potential causes for the reduction of the far-field noise. The variation in the correlation between spanwise velocity fluctuations for the porous leading edges, see Fig. 12, coupled with the decrease in the energy of the velocity fluctuations over the airfoil surface, see Fig. 14, indicates the probable causes for the far-field noise reduction. To complete the picture in the assessment of the airfoil response in relation to the far-field noise, the link between the surface pressure fluctuations and the far-field pressure

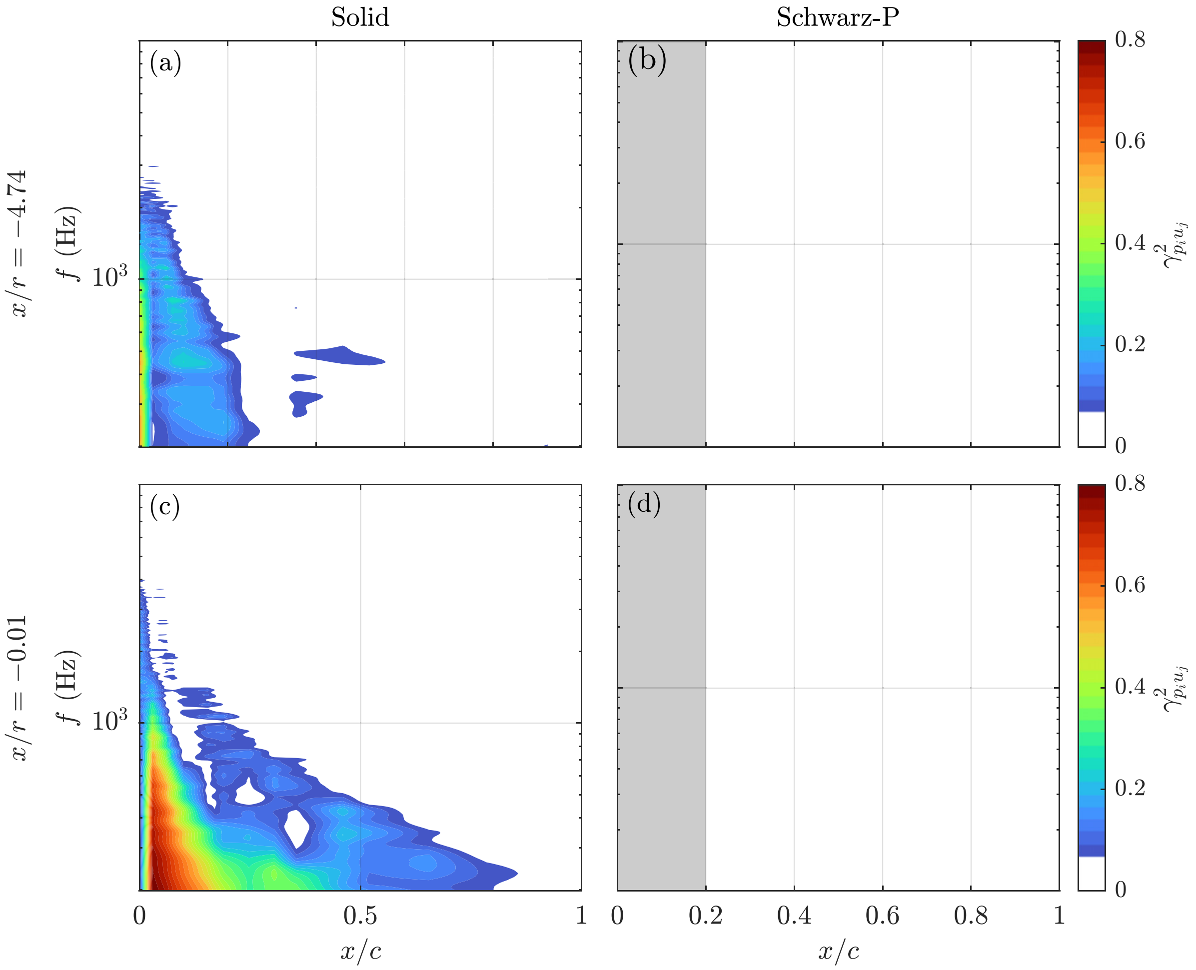

FIG. 15. Pressure–velocity magnitude-square coherence ($\gamma^2_{p_i u_j}$) between the surface pressure fluctuations measured over the airfoil and velocity fluctuations measured at $x/r = -4.74$ (top row) and $x/r = -0.01$ (bottom row) for solid [(a) and (c)] and Schwarz-P cases [(b) and (d)].

fluctuations (i.e., far-field noise) is examined via cross correlation analysis, Eq. (6), where the pressure fluctuations are obtained from the surface pressure transducers and the far-field microphone array.

The magnitude-squared coherence results for the solid leading edge case are presented first to set the frame to investigate the effect of the porous leading edge on the near-field to far-field coherence, see Fig. 16. Understanding the near-field to far-field coherence for the solid leading edge case is crucial to understand the achieved noise reduction from the implemented porous leading edges. The coherence results are presented for the surface pressure fluctuations over the airfoil, $0 < x/c < 0.92$, to far-field pressure fluctuations at the microphone located directly above the leading edge, $\theta = 90°$. The results are presented for three chordwise ranges, i.e., $0 < x/c < 0.21$, $0.24 < x/c < 0.46$, and $0.52 < x/c < 0.92$ [Figs. 16(a)–16(c)], to identify the role of each part of the airfoil on noise generation. A color is assigned to each transducer on the airfoil surface to ease the interpretation of the results, and the associated coherence curve is presented accordingly. As depicted in the figure, the level of near-field to far-field coherence increases from near-zero values at the stagnation point to elevated values over the leading edge of the airfoil, which then reduces approaching the trailing edge. It is of note that the near-field to far-field coherence is most significant over the region of $0.17 < x/c < 0.35$. Furthermore, the frequency range of the highest near-field to far-field pressure coherence coincides with the frequency range of the observed turbulence interaction noise. The near-field to far-field pressure coherence peaks between $100 < f < 200$ Hz and then quickly decays to a value above 0.1. Between $200 < f < 1000$ Hz, the level of coherence steadily decays as frequency increases. For the rear half of the airfoil presented, $0.52 < x/c < 0.92$, there is a strong low-frequency coherence at $x/c = 0.52$, which reduces toward the trailing edge. The chordwise locations near the trailing edge, $0.8 < x/c < 0.92$, demonstrate a small peak in the coherence at $f = 180$ Hz, which is likely caused by turbulent boundary layer interaction and the trailing edge.

Following the in-depth analysis of the coherence results for the solid leading edge case, a comparison study between the solid leading edge case to porous leading edge cases can be performed over the rest of the airfoil. Figure 17 presents the coherence results between the

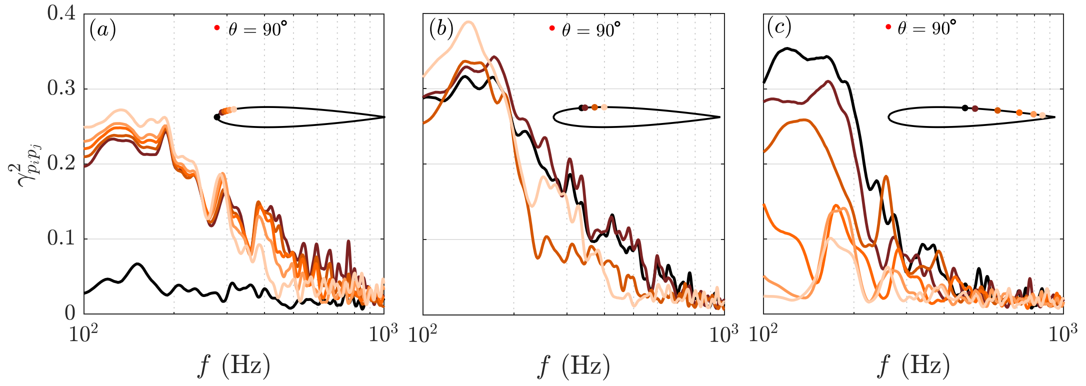

FIG. 16. Near-field to far-field magnitude-square coherence ($\gamma^2_{p_ip_j}$) between the far-field noise measured at $\theta = 90°$ to the surface pressure fluctuations measured over for the solid leading edge case, where (a) $0 < x/c < 0.16$, (b) $0.17 < x/c < 0.35$, and (c) $0.46 < x/c < 0.92$.

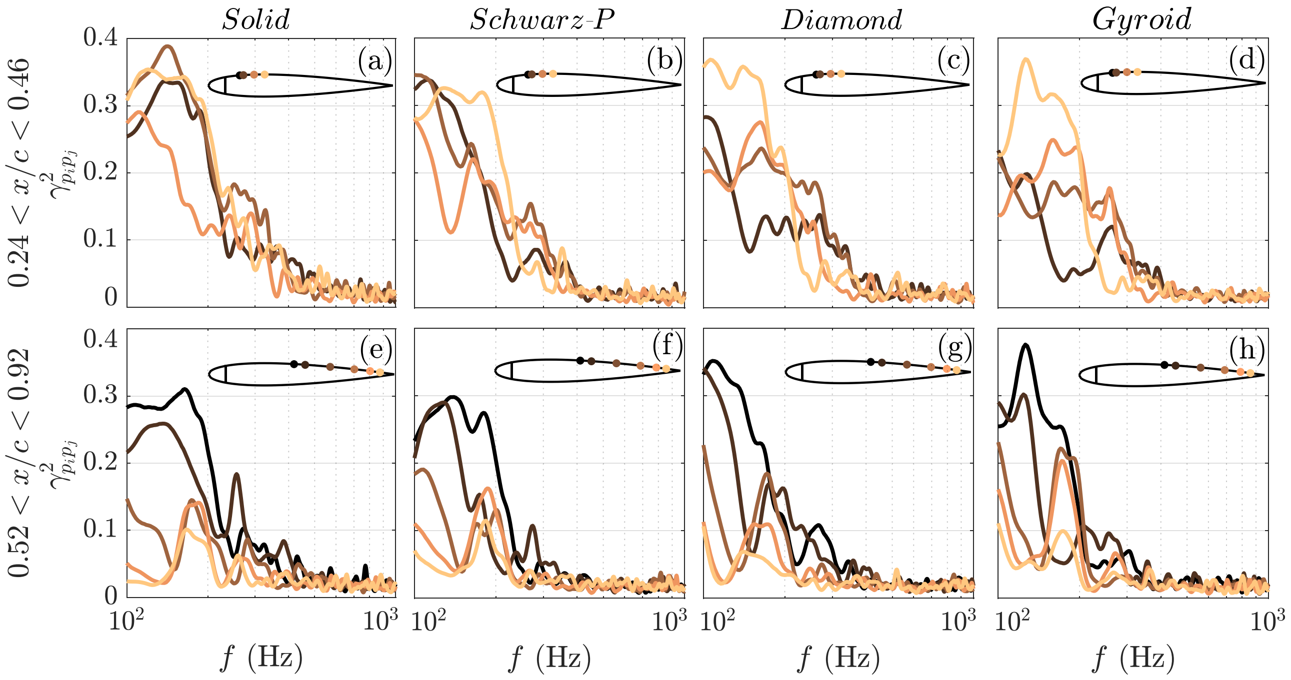

FIG. 17. Near-field to far-field magnitude-square coherence ($\gamma^2_{p_ip_j}$) between the far-field noise measured at $\theta = 90°$ to the surface pressure fluctuations at $0.24 < x/c < 0.46$ [(a)–(d)] and $0.52 < x/c < 0.92$ [(e)–(h)] for the solid and porous leading edges.

surface pressure fluctuations measured over $0.24 < x/c < 0.92$ to the far-field pressure fluctuations at the microphone located directly above the leading edge, $\theta = 90°$. To ease the interpretation, the results are presented for two chordwise ranges, $0.24 < x/c < 0.46$ (top row) and $0.52 < x/c < 0.92$ (bottom row), with a color assigned for each transducer on the airfoil. As previously explained, the solid leading edge case results demonstrate a strong coherence between the surface pressure fluctuations measured at the chordwise positions $0.24 < x/c < 0.46$ to the far-field noise. Considering the cases with porous leading edges, a significant decrease in the coherence values and the frequency range is evident for $0.24 < x/c < 0.46$. The magnitude-squared coherence results at the chordwise location $x/c = 0.24$ for the Schwarz-P case demonstrate an increase at around $f = 100$ Hz and a decay over $150 < f < 200$ Hz. For the same chordwise location, $x/c = 0.24$, the coherence level further decreases for the diamond and gyroid cases, which peaks below 0.3, coupled with a reduced range of frequency where coherence is evident. Considering the results over $0.52 < x/c < 0.92$, the porous leading edge treatment reduces the frequency range where the coherence is observed. However, coherence increases at $f < 150$ Hz for the diamond and gyroid leading edge cases. All the porous leading edges demonstrate a peak in the near-field to far-field coherence close to the trailing edge. Furthermore, the coherence magnitude is higher for the gyroid treatment case than the solid leading edge case. This peak observed in the results of the porous leading edges may emerge due to the increased level of shearing in the boundary layer, demonstrated in the results of the pressure fluctuations. It is important to note that for this frequency, the airfoil turbulence interaction noise is the dominant noise source, as discussed in Fig. 7.

IV. CONCLUSION

This study comprises experimental findings regarding the effect of mathematically defined leading edge porous treatments on reducing turbulence interaction noise. Three triply periodic minimal surface structures were selected, namely, Schwarz-P, gyroid, and diamond. The porous treatment occupies the first 10% of the airfoil leading edge with the same porosity, $\varphi = 50\%$. The porous leading edges demonstrate a marked reduction of the airfoil turbulence interaction noise at low frequencies. Despite their significantly different base structures, the Schwarz-P and gyroid structure leading edges demonstrated comparable performance in noise reduction. For all cases, a high-frequency penalty arises in alignment with the literature, which is addressed as surface roughness noise. Furthermore, the high-frequency increase in the narrowband spectra results does not significantly affect the overall sound pressure level significantly, as the noise reduction bares more weight due to its power level. Mathematically defined porous structures are shown to be an effective replacement of off the shelf porous materials and demonstrate far-field noise results in line with the literature. As it is possible to easily control the porosity and pore size of these porous structures, they would serve as an effective, tailored flow control method for the reduction of turbulence interaction noise. The gyroid leading edge structure demonstrates the most noise reduction potential when considering the results of the far-field noise.

Previous literature uses analysis of the flow along the stagnation streamline to characterize the noise reduction mechanisms, where one porous material type is generally studied. In this study, detailed analysis of the flow upstream of the porous leading edge for three different structure types revealed inconclusive to accurately describe the change in the flow physics responsible for the noise reduction. Velocity analysis along the stagnation line reveals that the effect of leading edge treatments alters the flow field in the proximity of the stagnation point. Furthermore, despite having the same porosity, the structure type significantly affects both the behavior of the mean flow and the velocity fluctuations in close proximity of the leading edge. An increase in the energy of the turbulent fluctuations near to the airfoil leading edge was evident in the Schwarz-P case compared with the solid leading edge, yet a reduction is observed for the diamond and gyroid leading edges.

Two-point velocity coherence analysis further demonstrates the different behavior of the turbulent structures near the porous leading edges, with the Schwarz-P leading edge displaying contrasting behavior compared to the diamond and gyroid structure leading edges results. Changes to the porous structure's bulk material properties could be attributed to the varying behavior of the turbulent structures at the leading edge based on the pore saturation of the turbulent structures. Interestingly, just off from the stagnation line, at the airfoil leading edge, all porous leading edges demonstrate a reduction in the low-frequency energy of the velocity fluctuations until approximately 50% of the porous section just off the surface of the airfoil. The reduction of the velocity fluctuation for each porous leading edge just off from the stagnation streamline, outside the boundary layer ($y/\delta_s > 10$), is the result that is most correlated with the far-field noise, as each porous leading edge demonstrates low-frequency reduction compared to the solid leading edge. At the point where the impedance jump from the materials occurs, from porous to solid, there is a significant increase in the high-frequency energy of the velocity fluctuations, which is likely a cause of the increased high-frequency noise.

Pressure–velocity coherence analysis shows that the strong communication between velocity and pressure for the solid leading edge case is completely attenuated by the introduction of the porous leading edge. Furthermore, near-field pressure to far-field pressure coherence is shown to be reduced over the solid part of the airfoil by the porous leading edges. The results demonstrate the importance of porous structure in attenuating the turbulence interaction noise. The results show that for a constant porosity, low-frequency noise reduction performance is achievable with a variety of porous architectures, and the increase in high-frequency noise can be reduced by choosing a structure with a smaller pore size. It is worth mentioning that both observations are also dependent on the inflow turbulence characteristics, i.e., length scale and turbulence intensity. A further study into the nature of the flow regarding its penetration into the porous material would help to identify the point of pore saturation and the turbulent eddies' interaction with the porous medium, which beyond the scope of this study.

ACKNOWLEDGMENTS

The first author (L.B.) would like to acknowledge the financial support of Embraer S.A. and an Engineering and Physical Sciences Research Council doctoral training partnership (EPSRC DTP). The second author (A.C.) was sponsored by EPSRC via Grant No. EP/S013024/1 at the University of Bristol from 1/6/2020 to 1/12/2022. All authors would like to acknowledge the financial support of EPSRC via Grant No. EP/S013024/1.

AUTHOR DECLARATIONS

Conflict of Interest

The authors have no conflicts to disclose.

Author Contributions

Luke Bowen: Conceptualization (equal); Data curation (equal); Formal analysis (equal); Investigation (equal); Methodology (equal); Visualization (lead); Writing – original draft (lead); Writing – review & editing (lead). **Alper Celik:** Conceptualization (equal); Data curation (equal); Formal analysis (equal); Investigation (equal); Methodology (equal); Supervision (supporting); Visualization (supporting); Writing – original draft (supporting); Writing – review & editing (equal). **Michelle Fernandino Westin:** Funding acquisition (supporting); Project administration (supporting); Supervision (supporting); Writing – review & editing (supporting). **Mahdi Azarpeyvand:** Conceptualization (equal); Funding acquisition (lead); Supervision (lead); Writing – review & editing (equal).

DATA AVAILABILITY

The data that support the findings of this study are available from the corresponding author upon reasonable request.

REFERENCES

[1] R. Amiet, "Acoustic radiation from an airfoil in a turbulent stream," J. Sound Vib. **41**, 407–420 (1975).

[2] S. Moreau and M. Roger, "Effect of angle of attack and airfoil shape on turbulence-interaction noise," AIAA Paper No. 2005-2973, 2005.

[3] W. J. Devenport, J. K. Staubs, and S. A. Glegg, "Sound radiation from real airfoils in turbulence," J. Sound Vib. **329**, 3470–3483 (2010).

[4] A. Celik, L. Bowen, and M. Azarpeyvand, "Unsteady aerodynamic response of a naca0012 in smooth and turbulent flows," AIAA Paper No. 2020-2600, 2020.

[5] A. Celik, L. Bowen, and M. Azarpeyvand, "Experimental investigation on the unsteady surface pressure fluctuation patterns over an airfoil," Phys. Fluids **34**, 105134 (2022).

[6] J. Gill, X. Zhang, and P. Joseph, "Symmetric airfoil geometry effects on leading edge noise," J. Acoust. Soc. Am. **134**, 2669–2680 (2013).

[7] J. R. Gill, X. Zhang, and P. Joseph, "Effects of real airfoil geometry on leading edge gust interaction noise," AIAA Paper No. 2013-2203, 2013.

[8] J. Gershfeld, "Leading edge noise from thick foils in turbulent flows," J. Acoust. Soc. Am. **116**, 1416–1426 (2004).

[9] F. V. Hutcheson, T. F. Brooks, and D. J. Stead, "Measurement of the noise resulting from the interaction of turbulence with a lifting surface," Int. J. Aeroacoust. **11**, 675–700 (2012).

[10] L. Bowen, A. Celik, M. Azarpeyvand, and C. R. I. da Silva, "Grid generated turbulence for aeroacoustic facility," AIAA J. **60**, 1833–1847 (2022).

[11] X. Liu, H. K. Jawahar, M. Azarpeyvand, and R. Theunissen, "Aerodynamic performance and wake development of airfoils with serrated trailing-edges," AIAA J. **55**, 3669–3680 (2017).

[12] Y. D. Mayer, B. Lyu, H. K. Jawahar, and M. Azarpeyvand, "A semi-analytical noise prediction model for airfoils with serrated trailing edges," Renewable Energy **143**, 679–691 (2019).

[13] H. K. Jawahar, Q. Ai, and M. Azarpeyvand, "Experimental and numerical investigation of aerodynamic performance for airfoils with morphed trailing edges," Renewable Energy **127**, 355–367 (2018).

[14] H. Kamliya Jawahar, S. A. Showkat Ali, and M. Azarpeyvand, "Serrated slat cusp for high-lift device noise reduction," Phys. Fluids **33**, 015107 (2021).

[15] A. Celik, Y. Mayer, and M. Azarpeyvand, "An experimental aeroacoustic study on serrated trailing-edge geometries and flow misalignment effects," AIAA Paper No. 2020-2518, 2020.

[16] B. Lyu and M. Azarpeyvand, "On the noise prediction for serrated leading edges," J. Fluid Mech. **826**, 205–234 (2017).

[17] A. Celik, Y. D. Mayer, and M. Azarpeyvand, "On the aeroacoustic characterization of a robust trailing-edge serration," Phys. Fluids **33**, 075120 (2021).

[18] S. A. Showkat Ali, M. Azarpeyvand, and C. R. Ilário da Silva, "Trailing-edge flow and noise control using porous treatments," J. Fluid Mech. **850**, 83–119 (2018).

[19] S. A. Showkat Ali, M. Azarpeyvand, M. Szőke, and C. R. Ilário da Silva, "Boundary layer flow interaction with a permeable wall," Phys. Fluids **30**, 085111 (2018).

[20] S. A. Showkat Ali, M. Azarpeyvand, and C. R. I. da Silva, "Trailing edge bluntness noise reduction using porous treatments," J. Sound Vib. **474**, 115257 (2020).

[21] A. R. Carpio, F. Avallone, and D. Ragni, "On the role of the flow permeability of metal foams on trailing edge noise reduction," AIAA Paper No. 2018-2964, 2018.

[22] E. J. G. Arcondoulis, T. F. Geyer, and Y. Liu, "An acoustic investigation of non-uniformly structured porous coated cylinders in uniform flow," J. Acoust. Soc. Am. **150**, 1231–1242 (2021).

[23] L. Bowen, A. Celik, M. Azarpeyvand, and C. R. da Silva, "Porous geometry effects on the generation of turbulence interaction noise," AIAA Paper No. 2021-2193, 2021.

[24] L. Bowen, A. Celik, M. Azarpeyvand, and M. F. Westin, "The effect of angle of attack on turbulence interaction noise with a porous leading edge," AIAA Paper No. 2022-3095, 2022.

[25] B. Lyu, M. Azarpeyvand, and S. Sinayoko, "Noise prediction for serrated leading-edges," AIAA Paper No. 2016-2740, 2016.

[26] J. Kim, S. Haeri, and P. Joseph, "On the reduction of aerofoil-turbulence interaction noise associated with wavy leading edges," J. Fluid Mech. **792**, 526–552 (2016).

[27] S. Narayanan, C. Paruchuri, S. Haeri, P. Joseph, J. W. Kim, and C. Polacsek, "Airfoil noise reductions through leading edge serrations," Phys. Fluids **27**, 025109 (2015).

[28] C. Paruchuri, P. Joseph, S. Narayanan, C. Vanderwel, J. Turner, J. W. Kim, and B. Ganapathisubramani, "Performance and mechanism of sinusoidal leading edge serrations for the reduction of turbulence-aerofoil interaction noise," J. Fluid Mech. **818**, 435–464 (2017).

[29] R. Chanaud, N. Kong, and R. Sitterding, "Experiments on porous blades as a means of reducing fan noise," J. Acoust. Soc. Am. **59**, 564 (1976).

[30] S. Lee, "Reduction of blade-vortex interaction noise through porous leading edge," AIAA J. **32**, 480–488 (1994).

[31] A. Tinetti, J. Kelly, R. Thomas, and S. Bauer, "Reduction of wake-stator interaction noise using passive porosity," AIAA Paper No. 2002-1036, 2002, p. 1036.

[32] T. Geyer, E. Sarradj, J. Giesler, and M. Hobracht, "Experimental assessment of the noise generated at the leading edge of porous airfoils using microphone array techniques," AIAA Paper No. 2011-2713, 2011.

[33] T. Geyer, E. Sarradj, and J. Giesler, "Application of a beamforming technique to the measurement of airfoil leading edge noise," Adv. Acoust. Vib. **2012**, 905461.

[34] E. Sarradj and T. Geyer, "Noise generation by porous airfoils," AIAA Paper No. 2007-3719, 2007.

[35] M. Roger, C. Schram, and L. D. Santana, "Reduction of airfoil turbulence-impingement noise by means of leading-edge serrations and/or porous material," AIAA Paper No. 2013-2108, 2013.

[36] M. Roger and S. Moreau, "Airfoil turbulence-impingement noise reduction by porosity or wavy leading-edge cut: Experimental investigations," in *Proceedings of the INTER-NOISE and NOISE-CON Congress and Conference* (Institute of Noise Control Engineering, 2016), Vol. 253, pp. 6366–6375.

[37] S. Satcunanathan, M. H. Meinke, and W. Schroeder, "Prediction of noise mitigation by porous media based on a direct-hybrid cfd/caa method," AIAA Paper No. 2019-2696, 2019, p. 2696.

[38] R. Zamponi, S. Satcunanathan, S. Moreau, D. Ragni, M. Meinke, W. Schröder, and C. Schram, "On the role of turbulence distortion on leading-edge noise reduction by means of porosity," J. Sound Vib. **485**, 115561 (2020).

[39] T. F. Geyer, A. Lucius, M. Schrödter, M. Schneider, and E. Sarradj, "Reduction of turbulence interaction noise through airfoils with perforated leading edges," Acta Acust. united Acust. **105**, 109–122 (2019).

[40] T. Sinnige, B. D. Corte, R. De Vries, F. Avallone, R. Merino-Martínez, D. Ragni, G. Eitelberg, and L. L. M. Veldhuis, "Alleviation of propeller-slipstream-induced unsteady pylon loading by a flow-permeable leading edge," J. Aircr. **56**, 1214–1230 (2019).

[41] S. Palleja-Cabre, C. C. Paruchuri, P. Joseph, M. J. Priddin, and L. J. Ayton, "Downstream perforations for the reduction of turbulence-aerofoil interaction noise. I. Experimental investigation," AIAA Paper No. 2021-2149, 2021.

[42] M. J. Priddin, L. J. Ayton, S. Palleja-Cabre, P. Chaitanya, and P. Joseph, "Downstream perforations for the reduction of turbulence-aerofoil interaction noise. II. Theoretical investigation," AIAA Paper No. 2021-2147, 2021.

[43] L. Bowen, A. Celik, M. Azarpeyvand, and C. R. I. da Silva, "On the use of tailored permeable surfaces for turbulence interaction noise control," AIAA Paper No. 2020-2530, 2020.

[44] C. Ocker, T. F. Geyer, F. Czwielong, F. Krömer, W. Pannert, M. Merkel, and S. Becker, "Permeable leading edges for airfoil and fan noise reduction in disturbed inflow," AIAA J. **59**, 4969–4986 (2021).

[45] L. Bowen, A. Celik, B. Zhou, M. F. Westin, and M. Azarpeyvand, "The effect of leading edge porosity on airfoil turbulence interaction noise," J. Acoust. Soc. Am. **152**, 1437–1448 (2022).

[46] Y. D. Mayer, H. K. Jawahar, M. Szőke, S. A. S. Ali, and M. Azarpeyvand, "Design and performance of an aeroacoustic wind tunnel facility at the university of bristol," Appl. Acoust. **155**, 358–370 (2019).

[47] Y. Mayer, B. Zang, and M. Azarpeyvand, "Near-field aeroacoustic characteristics of a stalled naca 0012 aerofoil," in *Proceedings of the 23rd International Congress on Acoustics, Integrating 4th EAA Euroregio* (Deutsche Gesellschaft fur Akustik, Aachen, Germany, 2019), pp. 5421–5428.

[48] A. P. G. Sagrado, "Boundary layer and trailing edge noise sources," Ph.D. thesis (University of Cambridge, 2008).

[49] L. Bowen, "Flow control using tailored permeable surfaces," Ph.D. thesis (University of Bristol, 2023).

[50] P. F. Mish, "An experimental investigation of unsteady surface pressure on single and multiple airfoils," Ph.D. thesis (Virginia Tech, 2003).

[51] S. A. Showkat Ali, "Flow over and past porous surfaces," Ph.D. thesis (University of Bristol, 2018).

[52] M. T. Szoke, "Trailing edge noise control using active flow control methods," Ph.D. thesis (University of Bristol, 2019).

[53] C. W. V. Atta and W. Y. Chen, "Correlation measurements in grid turbulence using digital harmonic analysis," J. Fluid Mech. **34**, 497–515 (1968).

[54] D.-J. Yoo, "Computer-aided porous scaffold design for tissue engineering using triply periodic minimal surfaces," Int. J. Precis. Eng. Manuf. **12**, 61–71 (2011).

[55] D. J. Yoo, "Porous scaffold design using the distance field and triply periodic minimal surface models," Biomaterials **32**, 7741–7754 (2011).

[56] M. Fantini, M. Curto, and F. De Crescenzio, "Tpms for interactive modelling of trabecular scaffolds for bone tissue engineering," in *Advances on Mechanics, Design Engineering and Manufacturing: Proceedings of the International Joint Conference on Mechanics, Design Engineering & Advanced Manufacturing (JCM)*, 14–16 September 2016, Catania, Italy (Springer, 2017), pp. 425–435.

[57] H. Schwarz, *Über Minimalflächen, Monatsber* (Berlin Akad, 1865).

[58] A. H. Schoen, *Infinite Periodic Minimal Surfaces without Self-Intersections* (National Aeronautics and Space Administration, 1970).

[59] B. Antohe, J. Lage, D. Price, and R. Weber, "Experimental determination of permeability and inertia coefficients of mechanically compressed aluminum porous matrices," ASME J. Fluid Eng. **119**, 404–412 (1997).

[60] F. Jørgensen, "How to measure turbulence with hot-wire anemometers—A practical guide," Skovlunde: Dantec Dynamics, Publication no. 9040U6151 (2 January 2002).

[61] P. Welch, "The use of fast Fourier transform for the estimation of power spectra: A method based on time averaging over short, modified periodograms," IEEE Trans. Audio Electroacoust. **15**, 70–73 (1967).

[62] L. D. Santana, J. Christophe, C. Schram, and W. Desmet, "A rapid distortion theory modified turbulence spectra for semi-analytical airfoil noise prediction," J. Sound Vib. **383**, 349–363 (2016).

[63] R. Zamponi, N. V. de Wyer, and C. F. Schram, "Experimental investigation of airfoil turbulence-impingement noise reduction using porous treatment," AIAA Paper No. 2019-2649, 2019.

[64] J. Isaza, R. Salazar, and Z. Warhaft, "On grid-generated turbulence in the near- and far field regions," J. Fluid Mech. **753**, 402–426 (2014).

[65] P. H. Westfall, "Kurtosis as peakedness, 1905–2014. rip," Am. Stat. **68**, 191–195 (2014).

[66] W. J. Devenport, D. L. Grissom, W. Nathan Alexander, B. S. Smith, and S. A. Glegg, "Measurements of roughness noise," J. Sound Vib. **330**, 4250–4273 (2011).

[67] L. Bowen, A. Celik, and M. Azarpeyvand, "A thorough experimental investigation on aerofoil turbulence interaction noise," Phys. Fluids **35**, 035123 (2023).